Spatial Dynamics of Myeloid-Tumor Cell Interactions During Early Non-Small Adenocarcinoma Development

Arie Gurin[1], Peter Manosalvas[2], Luis Perez[3], Henry Secaira[2], Caleb Ignace[4], Viswanathan Arunachalam[6], Carlos Castillo-Garsow[1], and Adrian Smith[5]

[1]Eastern Washington University, Cheney, Washington, USA
[2]Yachay Tech University, Urcuqui, Ecuador
[3]California Lutheran University, Thousand Oaks, California, USA
[4]Arizona State University, Tempe, Arizona, USA
[5]Benedictine University, Mesa, Arizona, USA
[6]Universidad Nacional de Colombia, Bogotá, Colombia

Abstract

Lung cancer yields the greatest mortality rate of all cancers in the United States. Among the types of lung cancer, non-small cell adenocarcinoma occurs most commonly in non-smokers. The immune system is the body's first response to abnormal cell behavior. However, tumor progression often evades the immune system's response and grows uncontrollably. This is a result of both tumor self-defense mechanisms inhibiting the maturation of myeloid cells in the environment, and/or natural spatial barriers of clumped tumor mass. We use a stochastic Cellular Automaton (CA) model to study the spatial dynamics of the immune cells (myeloid cells and T-cells) in response to tumor progression. This research explores how local effects of tumor defense mechanisms affect the spatial dynamics of tumor growth in terms of myeloid cell maturation and tumor proliferation. The mathematical analysis includes a mean-field approximation (MF) through a system of ordinary differential equations. The MF model is a non-spatial approximation to the spatially explicit Cellular Automaton model. We use numerical simulations to explore the control and growth of tumor progression. The results suggest that it is insufficient for mature myeloid cell quantities to surpass tumor cell quantities in order to eradicate tumor cells or vice versa.

1 Introduction

Cancer is a term referred to as a set of diseases that are capable of sustaining proliferative signaling, resisting cell death, evading tumor suppressors, inducing angiogenesis, enabling replicative immortality, initiating cellular invasion and metastasis [17]. A healthy cell can become cancerous by mutations to its genes. Gene mutation of a healthy cell results in uncontrolled and malicious behavior [17]. This may involve uncontrolled proliferation of the cell, disruption in its life cycle and growth, which leads to a tumor. A tumor is a mass of cells with abnormal morphological and molecular features [19, 35]. Malignant tumors spread to adjacent tissues and travel through the bloodstream and the lymphatic system to reach distant organs. Cancers are classified according to their tissue of origin [20, 26]. Cancers that arise in the epithelial tissue, one of the four basic tissues of the human body, are known as carcinomas. For example, non-small adenocarcinoma arises in the alveolar epithelium tissue [18, 26].

Lung cancer is the deadliest cancer according to the American Cancer Society [3]. Lung cancer disrupts the healthy function of the human body by having the patient experience constant cough, sputum streaked with blood, chest pain, breathing difficulty, and recurrent pneumonia or bronchitis [3]. It can be diagnosed as two types: Non-Small Cell Lung Cancer (NSCLC) and Small Cell Lung Cancer (SCLC). The NSCLC constitutes 80-85% of lung cancer patients and the remainder corresponds to the SCLC. Approximately 45% of lung patients have 1-year relative survival rate and only 16% of them are diagnosed at an early stage. Moreover, about 40% of patients diagnosed with NSCLC are more likely to get a subtype of cancer known as adenocarcinoma. This type of

cancer starts in the alveolar type-II cell, an epithelial cell with the function of secreting a protein known as surfactant [18]. The lung surfactant directs the gas-exchange mechanism and reduces the surface tension, which is essential for breathing [18].

The immune system detects and kills pathogens such as bacteria, viruses, parasites, and fungi. It is also capable of detecting and killing the body's own cells that contain abnormalities due to an illness or mutation such as cancer cells [1, 2]. The interaction between the immune system and cancer development has revealed that both the innate and adaptive immune system are involved in tumor recognition [12]. The relationship between both cells can be described with the hypothesis of cancer immunosurveillance which explains how tumor cells acquire mutations that allows them to avoid being targeted by the immune system [13]. This process is known as cancer immunoediting, which consists of three phases: elimination of abnormal cells, the equilibrium phase where the outgrowth of survivor tumor cells are controlled by the immune system and the escape phase where tumor cells are capable of avoiding immune system surveillance [6].

Moreover, recruitment of immature myeloid cells (ImC) and secretion of versican, an extracellular matrix component, by tumor cells trigger myeloid maturation [15, 22]. Upon maturation, mature myeloid cells (MmC), such as macrophages and dendritic cells, can recognize specific ligands on tumor cells and present tumor cell-derived molecules to T-cells ($CD4^+$ and $CD8^+$). Activation of T-cells leads to the elimination of tumor cells by secretion of granzyme and perforin. However, tumor cells that avoid the surveillance of immune system are able to release cytokines such as G-CSF, M-CSF, VEGF and IL-3 in order to suppress myeloid cell maturation [5, 13, 14, 22, 28, 31]. Cancer cells use this as a defense mechanism to evade the immune system by decreasing the production of mature myeloid cells in the body [5, 28].

Mathematical modeling of tumor growth has shown that the immune system has a vital role in phenomena such as oscillations in tumor size, tumor inactivity, and spontaneous growth regression [8]. While the modeling of the immune response against tumor started in 1986, a mechanistic understanding from a spatial dynamics approach continues to lack [7]. The inhibition mechanism that alters the balance between ImC and MmC has been studied to consider the interaction between the tumor and the immune system. Kareva, Berezovkaya, and Castillo-Chavez [22] proposed a system of ordinary differential equations (ODEs) to describe the growth rate changes of $CD8^+$ T-cells, tumor cells, ImC, and MmC. Research suggests that when the number of tumor cells is low and the immune system is strong enough, a patient can recover without treatment. Taking Kareva, Berezovkaya, and Castillo-Chavez work as baseline, we incorporate a new element on the study of tumor dynamics, empty space, which represents the impact of the available space left by a cell after its death, which has not been theoretically studied [9].

The secretion of cytokines by tumor cells in the alveolar epithelium have spatial local effects such as the inhibition of ImC maturation and the alteration of the immune cell's role in killing tumor cells from the tissue. Moreover, it is important to consider the spatial effects that cytokines have on the interaction between tumor cells and the immune system and the empty space that a cell can occupy.

Since the ODEs proposed in [22] do not describe local spatial interactions, we consider the implementation of a stochastic Cellular Automaton model. Also, the CA model explores how local effects of tumor defense mechanisms influence the spatial dynamics of tumor growth. These effects are studied through the mean-field approximation approach of the stochastic Cellular Automaton model through the local stability analysis of one tumor free equilibria (TFE). In order to simulate the spatial dynamics of the immune response interaction, we consider the transition probabilities from one state to another state occurring on a lattice with cardinal neighbors. In section 2, we describe both models. In Section 3, we present the mathematical analysis of the mean-field approximation. In section 4, we present the results of the CA and MF simulations. In section 5, we discuss the conclusion and implications of the project.

2 Methods

We use a Continuous-Time Markov Chain Cellular Automaton model with toroidal boundary conditions in a two dimensional lattice to simulate the early stage of NSCLC adenocarcinoma based on eight events governed by rules. In addition, we use a deterministic mean-field approximation through ODEs, which grants us qualitative understandings of the system.

2.1 Stochastic Cellular Automaton Model

Our approach is based on a Continous-Time Markov Chain (CTMC) stochastic Cellular Automaton where the events are independent and the waiting time between each event is distributed exponentially. Namely, we consider a continuous-time Poisson process for the transition events. In order to model the spatial dynamics of the myeloid-tumor cells interactions, the cells interact within a Von Neumann neighborhood.

The states E, T, M_1 and M_2 are the compartments that correspond to empty space, tumor cell, immature myeloid cells and mature myeloid cells, respectively. The transition rate between each state is shown in Figure 1. In Table 1, each parameter represents the rate in which an element of each state can transition to a different state. Note that the transition events associated with the parameters β, λ and θ depends on neighboring states of T^C, T, and M_2. Here, T^C represents all the non-tumor states (E, M_1, M_2).

We use a stochastic Cellular Automaton (CA) model with toroidal boundary conditions to avoid boundary effects in simulations. Our CA model considers a two dimensional lattice since the tissue we are modeling (i.e. the epithelial tissue in the alveolus) is one cell thick. In addition, for early stages of NSCLC adenocarcinoma, there is only tumor cell growth in the specified tissue. The simulation time is governed by the continuous time Poisson process in a markov chain. Waiting times between events has an underlying exponential probability distribution with parameter T_R (sum of rates from all possible events) [27]. The simulation is limited to one event happening at a time. In addition, every simulation begins with at least one tumor cell, and the placement of tumor cells on the lattice is clumped in order to create the tumor's "massed" nature. The relation of each cell is compared with its four neighbors in the form of the von Neumann neighborhood [27]. The CA is based on the transition events described in equations (1) - (8).

Table (1) Parameters associated to each transition event

Parameters	Description	Value	Source
α	Migration of ImC in response to tumor cells	100 day^{-1}	Estimated
ψ_1	Natural death of ImC	0.02 day^{-1}	[22]
θ	Maturation of ImC to MmC	0.02 day^{-1}	Estimate
ψ_2	Natural death of MmC	0.02 day^{-1}	[22]
λ	Proliferation of tumor cells	0.432 day^{-1}	[10]
ψ_T	Natural death of tumor cells	0.02 day^{-1}	[22]
β	Tumor death induced by MmC	0.0202 day^{-1}	Estimate
κ_1	Natural in-flow of ImC	10 day^{-1}	Estimate
κ_2	Natural out-flow of ImC	10 day^{-1}	Estimate
g	Inhibition of maturation of ImC by tumor cells	0.00125 day^{-1}	Estimate
b	Migration of ImC at half the maximum rate	$\frac{n^2}{5}$	Estimate

Let $R_{ij\to ii}$ denote the rate at which an **ij** pair becomes an **ii** pair. Let $R_{i\to j}$ denote the rate at which **i** cells become **j** cells in the lattice. Let N_{ij} denote the number of **j** cells that are part of an **ij** pair. We now give the following transition rates for the CA:

$$R_{TE\to TT} = \lambda N_{TE} \tag{1}$$
$$R_{E\to M_1} = E(\alpha T/(b+T) + \kappa_1) \tag{2}$$
$$R_{TM_1\to TM_2} = (\theta - g)N_{TM_1} \tag{3}$$
$$R_{T^cM_1\to T^cM_2} = \theta N_{T^cM_1} \tag{4}$$
$$R_{M_1\to E} = M_1(\psi_1 + \kappa_2) \tag{5}$$
$$R_{M_2\to E} = M_2\psi_2 \tag{6}$$
$$R_{M_2T\to M_2E} = \beta N_{M_2T} \tag{7}$$
$$R_{T\to E} = \psi_T T \tag{8}$$

where,

$$T_R = R_{E\to M_1} + R_{TE\to TT} + R_{T^cM_1\to T^cM_2} + R_{TM_1\to TM_2} + R_{M_1\to E} + R_{M_2\to E} + R_{M_2T\to M_2E} + R_{T\to E}$$

Note that,

$$T^c = \{E, M_1, M_2\}$$

and

$$N_{T^c M_1} = 4M_1 - N_{TM_1}$$

We take the probability of an event occurring by the rate of the event divided by the total rate. Rate (1) represents the tumor growth event that depends on the number of TE pairs times tumor cell proliferation, λ. Rate (2) represents the tumor-dependent migration and natural inflow of ImC. Note that for the tumor dependent migration rate given by $E[\alpha \frac{T}{b+T}]$, as $T \to \infty$, $\frac{T}{b+T} \to 1$. This means that α also represents the maximum rate of immature myeloid migration and b is the number of tumor cells at which the immune system sends immature myeloid cells at half the maximum rate. The natural inflow of ImC only considers the number of E cells in the lattice because it is not dependent on neighboring states. Rate (3) represents the tumor-dependent maturation, which is dependent on the number of TM_1 pairs multiplied by $(\theta - g)$. We only consider $\theta \geq g$ because we want to make sure that the natural maturation of ImC is greater than the inhibition of maturation of ImC by the presence of tumor cells. Rate (4) represents the natural maturation of ImC, which is dependent on the number of $T^C M_1$ pairs. This event takes the number of $T^C M_1$ pairs times the transition rate θ. Rate (5) represents the natural death of an ImC. Rate (6) represents the natural death of an MmC. Rate (8) represents the natural death of a tumor cell. Notice how rates (5,6,8) only depend on the quantity of the specified state multiplied by the parameter of the event (See Table 1). Finally, rate (7) represents the death of a tumor cell by an MmC, which is dependent on the number of M_2T pairs. This rate is evaluated by the number of M_2T pairs times the transition rate θ.

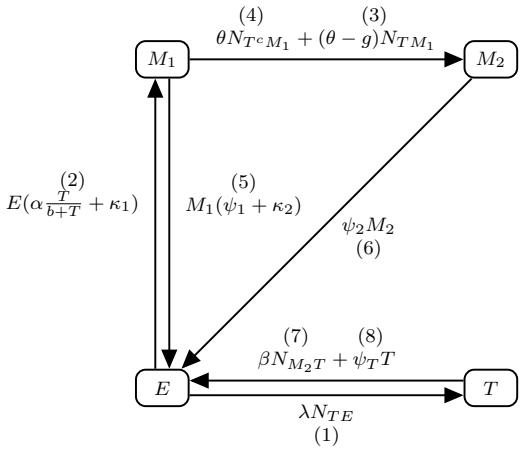

Figure (1) Flowchart of the State Variables

Parameter g represents the difference between the tumor's influence on immature myeloid cells and the stimulation of the immune system on the maturation rate of immature myeloid cells [22]. Let g_1 denote tumor influence delaying maturation of immature myeloid cells and g_2 denote immune system influence on maturation of immature myeloid cells. We have that g is given by $g = g_1 - g_2$. If g is negative, that means that the immune system has a stronger influence on myeloid cells' maturation. Otherwise, tumor cells have a much greater inhibition influence on the maturation of myeloid cells. Here, g_1 takes the form of activation suppression of ImC caused by the production of VEGF and other maturation-suppressing cytokines by the tumor[22]. The g_2 is a natural immune response to the presence of the tumor in the body that increases the stimulation of ImC maturation. Moreover, we consider just the case when $0 < g \leq \theta$ in order to increase the probability of the tumor dependent maturation event. This event is described by the rate (3).

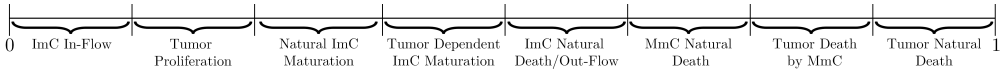

Figure (2) A visualization of the non-constant probability intervals that the Cellular Automaton algorithm chooses from to determine which event to execute next.

ImC flow into and out of the lungs as blood continues to circulate throughout the body. Also, inflow of ImC occurs when ImC identifies tumor cells [30]. If there are tumor cells and available space, then a random E is chosen and changed to an M_1. Our model simulates tumor proliferation but not cancerous cell growth [25]. The tumor proliferation event randomly selects a TE pair and updates the state E by T. Immature myeloid cells can mature to a mature myeloid cell as mentioned before. The natural maturation event randomly select a T^cM_1 pair and the M_1 changes to the M_2 state. On the other hand, ImC with a tumor neighbor have a lower probability of maturation because of the tumor defense mechanism [22]. The tumor-dependent maturation event randomly selects a TM_1 pair and the M_1 changes to the M_2 state.

Moreover, ImC naturally die due to programmed cell death [21]. The ImC natural death event randomly selects a M_1 and replaces it with an E state. Analogously, MmC are removed from a tissue due to programmed cell death [21]. The MmC natural death event randomly selects an M_2 and replacess M_2 with E. The MmC is able to identify tumor cells and secrete perforin \ granzyme to kill tumor cells[16]. The tumor death event by MmC randomly selects a M_2T pair and changes it by an empty space. The programmed cell death of tumor cells generate empty spaces that can become occupied [24]. The tumor natural death event randomly selects T and replaces it with E. The simulation rules for the CTMC Cellular Automaton are given as follows:

(A) The simulation begins with selection of a random event based on rates and total rate. Selection of random value between 0 and 1 satisfies that $r \sim U(0,1)$. The value r translates to the selection of an event represented in Figure 2.

(B) The simulation generates a random waiting time from an exponential distribution with parameter equal to the total rate. The time for the next event is given by $t_{i+1} = t_i + Exp(T_R(t_i))$.

(C) For the execution of the event, the i-th event is chosen if

$$r \in \left(\sum_{j=0}^{i-1} \mathrm{P}_j \ , \sum_{j=0}^{i} \mathrm{P}_j \right),$$

where event number 1 is associated with transition $E \to M_1$, event number 2 is associated with $TE \to TM_1$, and so on.

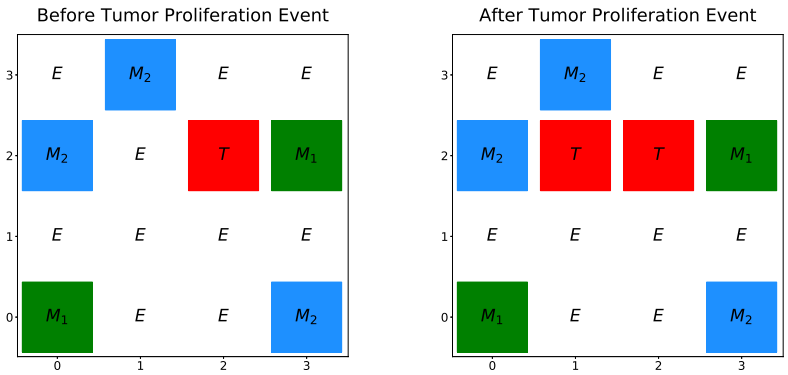

Figure (3) Tumor Proliferation Event. A portion of the lattice with the color coded of each state.

Furthermore, Figure 3 shows an example of a step in the simulation of the CA. In this example, the event that has been selected is tumor proliferation in which case, we consider the lattice screenshot to the left and the selection of a random TE pair (i.e. coordinates $(3,1) = E$ and $(3,2) = T$),

then the E in the TE pair is replaced with a T which is represented by the lattice screen-shot to the right.

2.2 Mean Field Approximation

A deterministic approach can be approximated through non-spatial interactions of the ImC, MmC, tumor cells, and empty space from the Markov chain states. The mean field (MF) approximation is given through the ODEs defined by the in-flows and out-flows of each state. Although the MF allows for mathematical analysis in order to gain qualitative understanding of the system, it does not consider local interaction such as spatial effects on the lattice. Instead, the MF approximation considers global interactions of the state variables and assumes a well mixing. Here, well mixing refers to different neighboring states of the center cell. Since the stochastic CA model considers the number of pairs, we need a different approach to incorporate the number of pairs into the MF model. For instance, we estimate the value of the number of TM_1 pairs by taking the proportion of tumor cells times the number of M_1 cells, this gives the final result, $(4\theta - g\frac{T}{N})M_1$. We used a similar approach for the other pairs described in the stochastic CA model (see Section 2.1).

$$\begin{aligned}
\frac{dE}{dt} &= (\psi_1 + \kappa_2)M_1 + \psi_2 M_2 + \beta T\frac{M_2}{N} + \psi_T T - \lambda T\frac{E}{N} - E(\alpha\frac{T}{b+T} + \kappa_1)\\
\frac{dM_1}{dt} &= E(\alpha\frac{T}{b+T} + \kappa_1) - (\psi_1 + \kappa_2)M_1 - (4\theta - g\frac{T}{N})M_1\\
\frac{dM_2}{dt} &= (4\theta - g\frac{T}{N})M_1 - \psi_2 M_2\\
\frac{dT}{dt} &= \lambda T\frac{E}{N} - \psi_T T - \beta T\frac{M_2}{N}
\end{aligned} \tag{9}$$

Due to the interactions between the MmC and tumor cells, this model agrees with biological assumptions such as the tumor-dependent migration of ImC, tumor death induced by MmC and the natural exchange flow of ImC. The main interactions between the myeloid and tumor cells are described in the flow chart below (See Figure 1). In addition, this model also represents the tumor defense mechanism that inhibits the maturation of the ImC. This is represented by the rate $4\theta - g\frac{T}{N}$. The approximation of tumor dependent maturation rate with TM_1 pairs is represented by the expression $g\frac{TM_1}{N}$. We conclude this result because of two possible ImC maturation events that can occur, the natural maturation rate and the tumor influenced maturation rate. The natural maturation rate is expressed as $\theta N_{T^C M_1}$ where the rate θ represents natural maturation which is dependent on the number of $T^C M_1$ pairs. Equivalently, the natural maturation rate can be expressed as $\theta(4M_1 - N_{TM_1})$. The tumor influenced maturation rate is expressed by $(\theta - g)N_{TM_1}$, where we take the difference between the rate of natural maturation and maturation in response to a tumor cell by the number of TM_1 pairs. Combining both of these equations results in the following expression: $4\theta M_1 - gN_{TM_1}$.

3 Mathematical Analysis

3.1 Mean Field Approximation: Equilibria and Stability

The total population is constant because we consider a fixed lattice size, we can take $N = E + M_1 + M_2 + T$ and solve for E (i.e. $E = N - M_1 - M_2 - T$) then substitute $E = N - M_1 - M_2 - T$ into our equations. Notice that the last three equations no longer have dependence on E, so we can reduce our 4D system to a 3D system by eliminating $\frac{dE}{dt}$. We then obtain:

$$\begin{aligned}
\frac{dM_1}{dt} &= (N - M_1 - M_2 - T)(\alpha\frac{T}{b+T} + \kappa_1) - (\psi_1 + \kappa_2)M_1 - (4\theta - g\frac{T}{N})M_1\\
\frac{dM_2}{dt} &= (4\theta - g\frac{T}{N})M_1 - \psi_2 M_2\\
\frac{dT}{dt} &= \lambda T\frac{(N - M_1 - M_2 - T)}{N} - \psi_T T - \beta T\frac{M_2}{N}
\end{aligned} \tag{10}$$

Next, we consider the Jacobian associated with the reduced system:

$$\begin{pmatrix} \frac{gT}{N} - \frac{\alpha T}{b+T} - 4\theta - \kappa_1 - \kappa_2 - \psi_1 & -\frac{T\alpha}{b+T} - \kappa_1 & \frac{gM_1}{N} + (-M_1 - M_2 + N - T)\left(\frac{\alpha}{b+T} - \frac{T\alpha}{(b+T)^2}\right) - \kappa_1 - \frac{T\alpha}{b+T} \\ 4\theta - \frac{gT}{N} & -\psi_2 & -\frac{gM_1}{N} \\ -\frac{T\lambda}{N} & -\frac{T\beta}{N} - \frac{T\lambda}{N} & -\frac{M_2\beta}{N} + \frac{(-M_1-M_2+N-T)\lambda}{N} - \psi_T - \frac{T\lambda}{N} \end{pmatrix}$$

Our Tumor Free Equilibrium is given by:

$$\left\{M_1 \to \frac{\kappa_1 \mathrm{N}\psi_2}{4\theta\kappa_1 + 4\theta\psi_2 + \kappa_1\psi_2 + \kappa_2\psi_2 + \psi_1\psi_2}, M_2 \to \frac{4\theta\kappa_1 \mathrm{N}}{4\theta\kappa_1 + 4\theta\psi_2 + \kappa_1\psi_2 + \kappa_2\psi_2 + \psi_1\psi_2}, T \to 0\right\}$$

Evaluating at the Tumor Free Equilibrium, we obtain the following matrix:

$$\begin{pmatrix} -4\theta - \kappa_1 - \kappa_2 - \psi_1 & -\kappa_1 & \frac{\mathrm{N}\alpha(4\theta+\kappa 2+\psi_1)\psi_2 + b\kappa_1(g\psi_2 - (\kappa_1+\kappa_2+\psi_1)\psi_2 - 4\theta(\kappa_1+\psi_2))}{4b\theta\kappa_1 + b(4\theta+\kappa_1+\kappa_2+\psi_1)\psi_2} \\ 4\theta & -\psi_2 & -\frac{g\kappa_1\psi_2}{(\kappa_1+\kappa_2+\psi_1)\psi_2 + 4\theta(\kappa_1+\psi_2)} \\ 0 & 0 & \frac{-4\beta\theta\kappa_1 + \lambda(4\theta+\kappa_2+\psi_1)\psi_2 - ((\kappa_1+\kappa_2+\psi_1)\psi_2 + 4\theta(\kappa_1+\psi_2))\psi_T}{(\kappa_1+\kappa_2+\psi_1)\psi_2 + 4\theta(\kappa_1+\psi_2)} \end{pmatrix}$$

with associated eigenvalues:

$$\begin{aligned} a_1 &= \frac{1}{2}\left(-\sqrt{16\theta^2 + 8\theta(-\kappa_1+\kappa_2+\psi_1-\psi_2) + (\kappa_1+\kappa_2+\psi_1-\psi_2)^2} - 4\theta - \kappa_1 - \kappa_2 - \psi_1 - \psi_2\right), \\ a_2 &= \frac{1}{2}\left(\sqrt{16\theta^2 + 8\theta(-\kappa_1+\kappa_2+\psi_1-\psi_2) + (\kappa_1+\kappa_2+\psi_1-\psi_2)^2} - 4\theta - \kappa_1 - \kappa_2 - \psi_1 - \psi_2\right), \\ a_3 &= \frac{-4\beta\theta\kappa_1 - \psi_T(4\theta(\kappa_1+\psi_2) + \psi_2(\kappa_1+\kappa_2+\psi_1)) + \lambda\psi_2(4\theta+\kappa_2+\psi_1)}{4\theta(\kappa_1+\psi_2) + \psi_2(\kappa_1+\kappa_2+\psi_1)}. \end{aligned} \tag{11}$$

According to the Routh-Hurwitz stability criterion, the tumor free equilibrium is stable if and only if all real parts of the eigenvalues are negative. In other words, the TFE is stable if and only if $a_2 < 0$ and $a_3 < 0$, i.e.

$$0 < \lambda \leq \frac{4\beta\theta\kappa_1}{\psi_2(4\theta+\kappa_2+\psi_1)} \quad \text{and} \quad \mid 4\theta + \kappa_1 + \kappa_2 + \psi_1 - \psi_2 \mid \ \geq 4\sqrt{\theta\kappa_1}.$$

We calculated the basic reproductive number (R_0) using the next generation operator [34]. When using the next generation method, we denote $x = \{x_1, x_2, ..., x_n\}$ to represent n tumorous host compartments and $y = \{y_1, y_2, ..., y_m\}$ to represent m other host compartments. In addition, we take the rate at which new tumor cells enter the compartment i as $\mathcal{F}_i$ and the transfer of cells out of and into the ith compartment as $-\mathcal{V}_i$. This is expressed as: $\frac{d\vec{x}}{dt} = \mathcal{F}_i - \mathcal{V}_i$.

$$\text{Then } F = \frac{d}{d\vec{x}}\mathcal{F}\Big|_{TFE} \text{ and } V = \frac{d}{d\vec{x}}\mathcal{V}\Big|_{TFE}.$$

We then express the rate at which individuals in compartment j generate new tumor cells in compartment i by the average length of time a cell spends in a single visit to compartment j as FV^{-1}. The R_0 is then given by the dominant eigenvalue for FV^{-1} (i.e. $\rho(FV^{-1})$). In our case, we obtain a single value for FV^{-1}, which is the resulting R_0 value.
Now, in our 3D system, $x = \{T\}$ and $y = \{E, M_1, M_2\}$ so $\mathcal{F} = \lambda T\frac{E}{N}$ and $\mathcal{V} = \psi_T T + \beta T\frac{M_2}{N}$. We then obtain F by evaluating the partial derivative of the x by the desired compartment $\frac{\partial(\lambda T\frac{E}{N})}{\partial T} = \lambda\frac{E^*}{N}$. Similarly, we obtain V^{-1} by evaluating the partial derivative of the y by the desired compartment: $\frac{\partial(\beta T\frac{M_2}{N} + \psi_T T)}{\partial T} = \beta\frac{M_2^*}{N} + \psi_T$. Then, by taking FV^{-1} we obtain the following:

$$R_0 = \frac{\lambda E^*}{N\psi_T + \beta M_2^*} \tag{12}$$

Now, we substitute values from the tumor free equilibrium:

$$R_0 = \frac{\lambda\psi_2(4\theta+\kappa_2+\psi_1)}{4\beta\theta\kappa_1 + 4\theta\psi_T(\kappa_1+\psi_2) + \psi_2\psi_T(\kappa_1+\kappa_2+\psi_1)}. \tag{13}$$

We perform some simplification of the R_0 to best interpret the biological meaning. Please refer to Appendix for the step by step simplification. The simplified R_0 result yields:

$$R_0 = \frac{\lambda}{\psi_T(R_{M_1} + R_{M_2}R_{M_1} + 1) + \beta R_{M_2}R_{M_1}}; \text{ where } \quad R_{M_1} = \frac{\kappa_1}{4\theta+\kappa_2+\psi_1}, R_{M_2} = \frac{4\theta}{\psi_2} \tag{14}$$

Hence, we can notice that the terms R_{M_2} and R_{M_1} are related with the quotients between the inflows and outflows of the states M_2 and M_1, respectively. These quotients represent the influence of the ImC and MmC on tumor growth. In other words, the increment of MmC and ImC results in the decrement of R_0 for tumor growth.
The quantity R_{M_2} is expressed as the quotient of natural maturation of myeloid cells (θ), and natural death of MmC, (ψ_2). For MmC to increase in quantity, their maturation rate must be 4 times faster than their death rate. On the other hand, the quantity R_{M_1} is expressed as the quotient of natural inflow of ImC into the system, (κ_1), to the sum of the rates of natural maturation rate of ImC, (θ), the outflow of ImC rate from the system, (κ_2), and the natural death rate of ImC, ψ_T. For ImC to increase in quantity, their inflow rate must be faster than 4 times the sum of natural maturation rate, outflow, and natural death rate.

In addition, the term $R_{M_1}R_{M_2}(\beta+\psi_T)$ represents the influence of the ImC and MmC rates to the tumor death outflows (natural and M_2 dependent death). Enough increment of the parameter θ results in the critical maturation of most myeloid cells, which can be interpreted as the effect of the immune system on the total outflow rate of tumor cells. In other words, this increment contributes decreasing the R_0 for a stable tumor free equilibria. Under the assumption that $R_{M_1} = R_{M_2} = 1$ we get $R_0 = \frac{\lambda}{3\psi_T+\beta}$, which means that under a uniform flow interchange of M_1 and M_2 the natural tumor death has more influence in the stability of the tumor free equilibria.

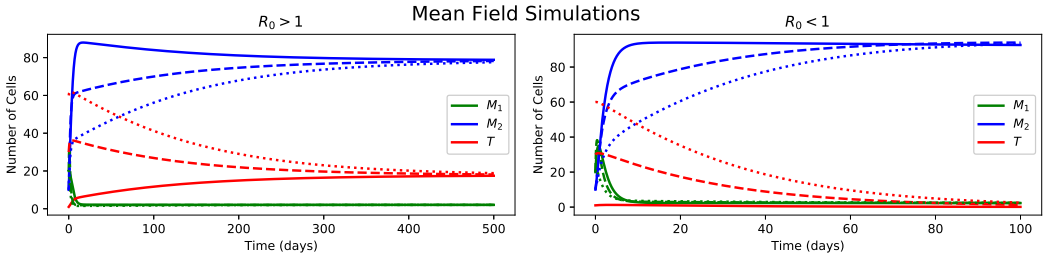

Figure (4) 10 x 10 Lattice. Initial Conditions: (1) $T_0 = 1, M_{1,0} = 20, M_{2,0} = 10$ (2) $T_0 = 30, M_{1,0} = 20, M_{2,0} = 10$ (3) $T_0 = 60, M_{1,0} = 20, M_{2,0} = 10$.
$R_0 < 1$. Parameter Values Used: $\alpha = 4, \psi_1 = 0.005, \theta = 0.2, \psi_2 = 0.02, \lambda = 0.4, \psi_T = 0.025, \beta = 0.015, \kappa_1 = 0.5, \kappa_2 = 0.5, g = 0.3, b = 5$.
$R_0 > 1$. Parameter Values Used: $\alpha = 4, \psi_1 = 0.01, \theta = 0.2, \psi_2 = 0.02, \lambda = 0.8, \psi_T = 0.005, \beta = 0.01, \kappa_1 = 0.2, \kappa_2 = 0.2, g = 0.2, b = 50$.

Figure 4 shows two simulations of the mean field approximation when $R_0 < 1$ and $R_0 > 1$, respectively. Notice that for all three realizations of $R_0 > 1$ for tumor growth, a steady-state endemic is achieved which is in agreement with the value of the R_0. In addition, all three realizations show that the ImC go to zero and that the MmC reach a steady-state by day 500 of the simulation. As for all three realizations of $R_0 < 1$ for the tumor, tumor death is achieved by day 100 which is in agreement with the value of the R_0. Also, we notice that the MmC reach a steady-state while ImC goes to zero.

4 Results

In this section, we present the results and a brief interpretation of the simulations for the CA model. We manipulated the default parameters of Table 1 to observe stochastic tumor endemic, tumor extinction, and tumor-myeloid coexistence scenarios through parameter sweep simulations.

4.1 CA Simulation: The Influence of lattice size on tumor size

In this project, we accounted for space as a major piece in the behavior of our system. A question we were concerned about included the effect of the lattice size (n) on the tumor cells' success rate at reaching steady-state. In other words, we wanted to address under what dimension of the lattice tumor is most likely to persist. We ran simulations using the Cellular Automaton in which the initial conditions of tumor cell quantity is one tenth of the lattice size. Figure 5 shows that the proportion of tumor cells at steady state, $\frac{T}{n^2}$, decreases as the lattice size increases. We can notice

that the behavior is similar to the function $f(x) = \frac{1}{x^2}$ which means that the steady states of the tumor cells do not present a significant change through an increment of the lattice size.

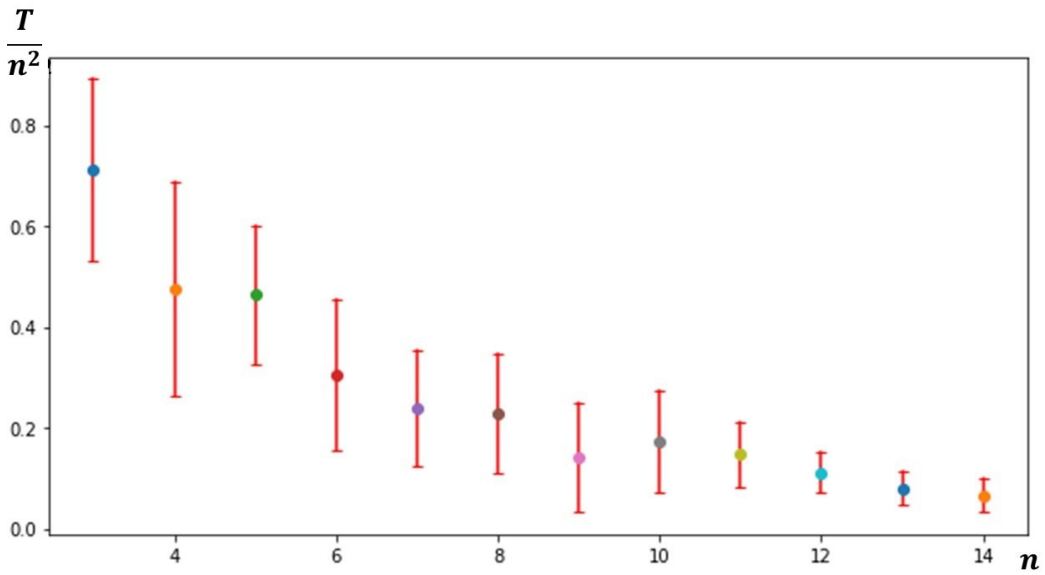

Figure (5) Proportion of tumor cells at steady-state with respect to n by n lattice size. Parameters used: $\alpha = 0.6, \psi_1 = 0.1, \theta = 0.9, \psi_2 = 0.1, \lambda = 0.9, \psi_T = 0.05, \beta = 0.05, \kappa_1 = 0.05, \kappa_2 = 0.05, g = 0.1, b = 3$

4.2 CA Simulation: Endemic Tumor

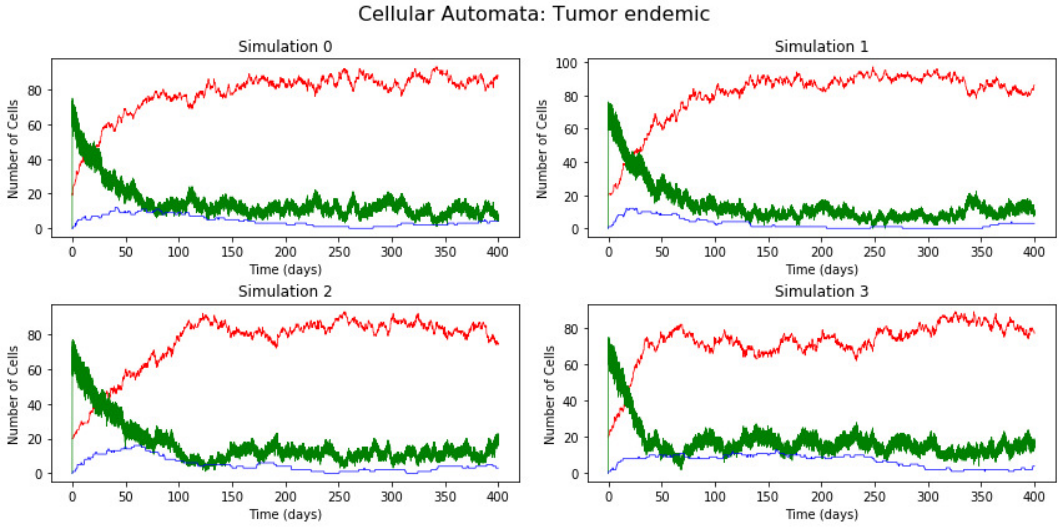

Figure (6) Endemic tumor spread during 400 days. Parameter values used: $b = \frac{10^2}{5}$, $g = 0.00125$, $\alpha = 100$, $\psi_1 = 0.02$, $\psi_2 = 0.02$, $\psi_T = 0.02$, $\beta = 0.0202$, $\lambda = 0.432$, $\theta = 0.002$, $\kappa_1 = 10$, and $\kappa_2 = 10$. The initial conditions are: $T_0 = 20$, $M_{1,0} = 0$, and $M_{2,0} = 0$. Size of of the lattice: 10 by 10. T cells: red, MmC: blue, ImC: green.

If the value of the natural maturation rate of ImC (θ) decreases, we expect tumor cells to proliferate without control because less MmC are available to kill tumor cells. This idea is confirmed by the results shown in Figure 6, in which tumor cells (red) reach a steady-state behavior towards the end of the 400 days. The MmC (blue) become extinct before the ImC because the number

of tumor cells increases rapidly and inhibit the maturation of ImC. In this scenario, the immune system is not sufficient to eradicate tumor cells. Also, note that the tumor cells reach a boundary condition given by the size of the lattice. In other words, this simulation represents tumor spread limited by the size of the tissue (lattice).

4.3 Tumor and Mature Myeloid Cells Coexistence

Coexistence between the myeloid cells and the tumor cells occurs when both persist in surviving and fail at eradicating each other despite increase and decrease in quantity throughout time. If the rate at which the tumor cells are killed by MmC (β) decreases, we expect to see an increase in the survival of tumor cells. This idea is confirmed by Figure 7, where we can see tumor-myeloid interactions for a small value of the parameter g, that is the inhibition of maturation of ImC by tumor cells. Hence, we can simulate an earlier stage of tumor growth expansion for the case when tumor cells evolve to avoid immunosurveillance. Moreover, in Figure 8, the tumor-myeloid cells interactions are shown in many different stochastic simulations. The coexistence behavior shows that the population size of ImC is almost eradicated which means that maturation is high when most of these cells are maturing. This trend continues throughout 5000 days.

Note that in Figure 7 the population of ImC does not undergo extinction compared to the ImC population of Figure 8. Indeed, in Figure 7 there is an interaction between tumor, MmC, and ImC, whereas in Figure 8 the only interaction that occurs is between tumor and MmC. Moreover, in Figure 8 the only events that occur are the natural death of MmC, the natural death rate of tumor cells, and tumor death by MmC. This explains why the interaction between tumor and MmC appear as mirror images of each other (See Figure 8).

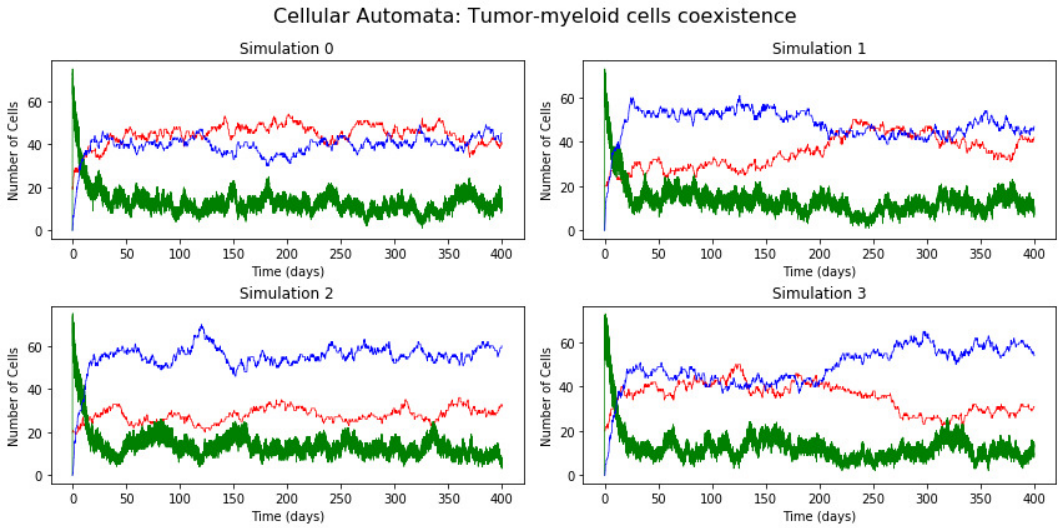

Figure (7) Tumor and myeloid Coexistence simulation. Size of lattice is 10 by 10, and parameter values are: $b = \frac{10^2}{5}$, $g = 0.00125$, $\alpha = 100$, $\psi_1 = 0.02$, $\psi_2 = 0.02$, $\psi_T = 0.02$, $\beta = 0.00202$, $\lambda = 0.432$, $\theta = 0.02$, $\kappa_1 = 10$, and $\kappa_2 = 10$. The initial conditions are: T=20, $M_1 = 0$, and $M_2 = 0$. With $b = \frac{n^2}{5}$ we obtain tumor extinction. T cells: red, MmC: blue, Imc: green.

4.4 CA Simulation: Tumor extinction

We run a simulation with the values of Table 2 and we obtained a scenario in which we expect to observe tumor extinction driven by MmC. As seen in Figure 9, tumor cells reach a peak approximately between the first to the fiftieth days interval and then undergoes extinction. Whereas the MmC increase, and the ImC population remains low but do not undergo extinction.

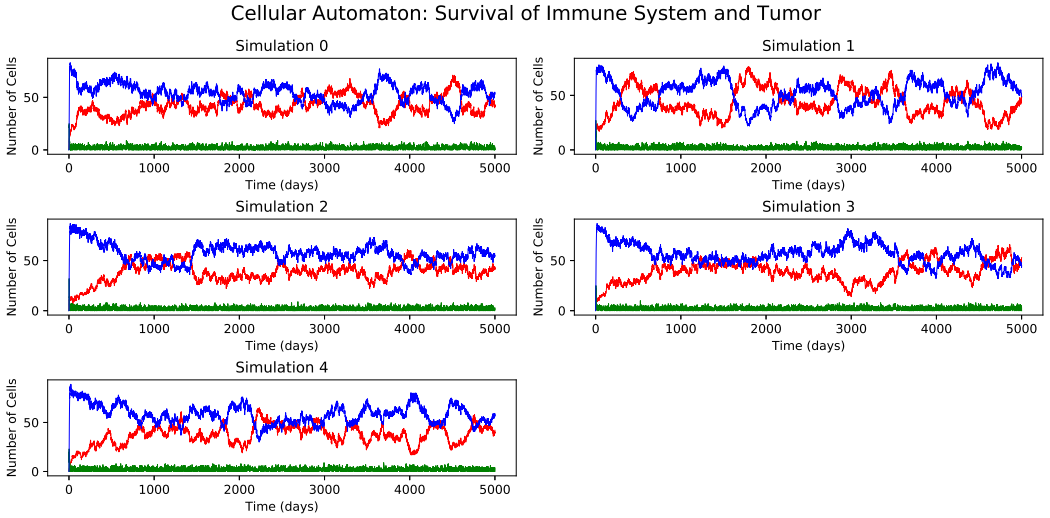

Figure (8) Five stochastic simulations for the tumor-myeloid cells interaction, using a 10 by 10 lattice and the following parameter values: $b = 10$, $g = 0.15$, $\alpha = 1$, $\psi_1 = 0.02$, $\psi_2 = 0.02$, $\psi_T = 0.015$, $\beta = 0.01$, $\lambda = 0.6$, $\theta = 0.2$, $\kappa_1 = 0.2$, and $\kappa_2 = 0.2$. The initial conditions are: $T_0 = 1$, $M_{1,0} = 0$, and $M_{2,0} = 0$. T cells: red, MmC: blue, ImC: green.

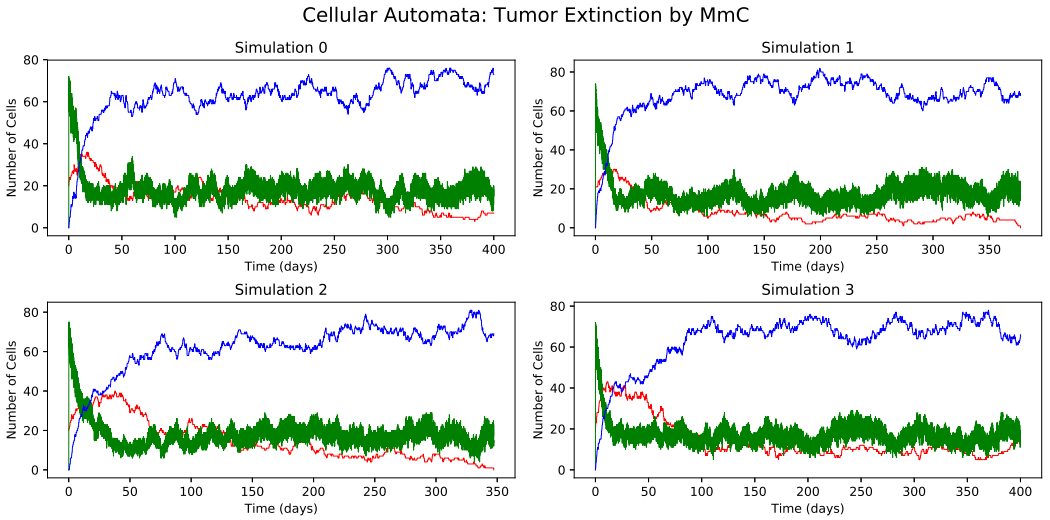

Figure (9) Tumor extinction by the immune system with a lattice size 10 by 10. Tumor = Red, ImC = Green, MmC = Blue. The parameter values used are the same as in Table 1. The initial conditions are: $T_0 = 20$, $M_{1,0} = 0$, and $M_{2,0} = 0$. T cells: red, MmC: blue, Imc: green.

4.5 Parameter Sweep

We identified the maturation rate of proliferation of tumor cells rate (λ), tumor induced death by MmC rate (β), ImC natural maturation (θ), and the natural in-flow of ImC (κ_1), as the most important parameters that affect the spatial dynamics of tumor progression. To observe the effects of each parameter on the tumor's behavior, we conducted simulations of parameter sweeps through the Cellular Automaton for each parameter mentioned above, and look at the relationship they have with the equilibrium states of T, M_1 and M_2.

Let's consider the parameter sweep of λ:

For the parameter sweep of λ in figure 10, the equilibrium values of each state were calculated by taking the end values of each realization. Three realizations were ran in this simulation. Recall that λ represents tumor growth. In addition, notice that the first two values selected to simulate, along with the other parameter values, create an R_0 value less than one. For these first two values,

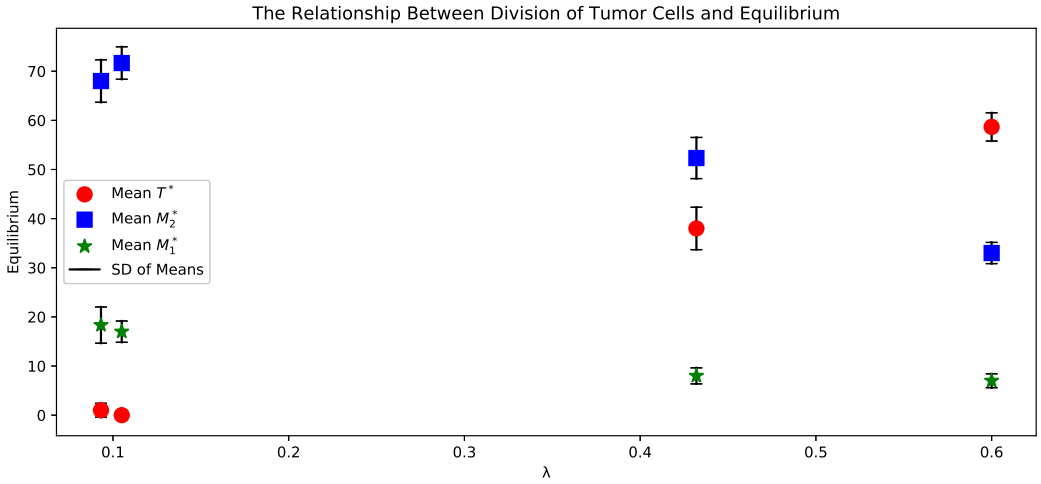

Figure (10) Parameter sweep on λ with values of 0.0932, 0.105, 0.432 and 0.6, using a 10 by 10 lattice size. End time = 500 days.
Parameter Values: $\alpha = 100$, $\psi_1 = 0.02$, $\psi_2 = 0.02$, $\lambda = 0.432$, $\psi_T = 0.02$, $\beta = 0.00202$, $\kappa_1 = 10$, $\kappa_2 = 10$, $b = \frac{n^2}{5}$, $\theta = 0.02$, $g = 0.00125$. Initial conditions: $T_0 = 20$, $M_{1,0} = 0$,$M_{2,0} = 0$. End Time = 500 days.

we notice a tumor free equilibrium. This is due to a lower tumor growth rate compared to the rate at which the states influence decay of tumor growth. The last two λ values along with the other parameter values indicate an R_0 greater than one. The resulting simulations indicate that the tumor equilibrium reaches an endemic. Here, the parameter sweep of λ results in the conclusion that the mean-field approximation is able to captivate the relation between tumor growth and the tumor equilibria; results also expressed via the Cellular Automaton (CA).

Let's now consider the parameter sweep of β:

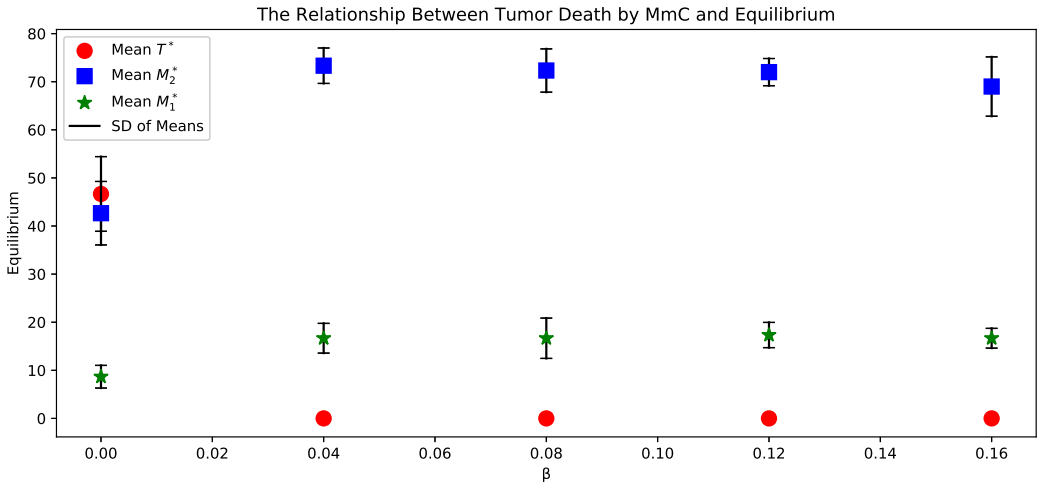

Figure (11) Parameter sweep on β with values between 0 and 0.16, using a 10 by 10 lattice size. End time = 500 days.
Parameter Values: $\alpha = 100$, $\psi_1 = 0.02$, $\psi_2 = 0.02$, $\lambda = 0.432$, $\psi_T = 0.02$, $\kappa_1 = 10$, $\kappa_2 = 10$, $b = \frac{n^2}{5}$, $\theta = 0.02$, $g = 0.00125$. Initial conditions: $T_0 = 20$, $M_{1,0} = 0$,$M_{2,0} = 0$. End Time = 500 days.

For the parameter sweep of β in figure 11, the equilibrium values of each state were calculated by taking the end values of each realization. Three realizations were ran in this simulation. Recall that the parameter β represents the death of a tumor by MmC. The first two values, along with

the values of the other parameters, create an R_0 value greater than one. The first value shows a clear case that the tumor equilibrium is endemic due to a greater rate for tumor growth compared to the rate at which tumor growth is inhibited. We notice here that the mean-field approximation is able to represent the behavior of this parameter on the tumor equilibrium. While the second β value indicates that the value of R_0 is greater than one, the simulation shows that there is a tumor free equilibrium. This contradicting information can be due to the mean-fields inability to capture the spatial effects that the CA expresses. The last three simulated values of β, along with the other parameter values, create an R_0 less than zero, which implies a tumor free equilibrium. This is due to a lower tumor growth rate compared to the rate at which other states influence decay of tumor growth. Let's now consider the parameter sweep of θ:

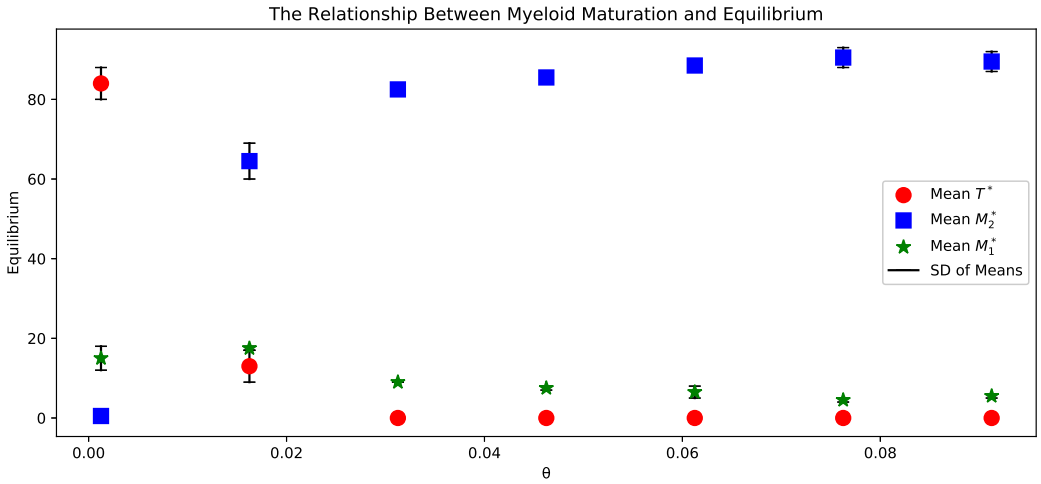

Figure (12) Parameter sweep on θ with a range from 0.00125 to 0.1, using 10 by 10 lattice size. Parameter Values: $\alpha = 100$, $\psi_1 = 0.02$, $\psi_2 = 0.02$, $\lambda = 0.432$, $\psi_T = 0.02$, $\beta = 0.0202$, $\kappa_1 = 10$, $\kappa_2 = 10$, $g = 0.00125$, $b = \frac{n^2}{5}$. Initial conditions: $T_0 = 20$, $M_{1,0} = 8$,$M_{2,0} = 4$. End Time = 500 days.

For the parameter sweep of θ in figure 12, the equilibrium values of each state were calculated by taking the end values of each realization. Two realizations were ran in this simulation. Recall that θ represents the rate of maturation of ImC. Notice how the increase in rate of the MmC and ImC makes the tumor equilibrium go to zero due to the increase in probability that a tumor dies by the influence of an MmC. This is justified by the increase in the equilibrium of MmC as evidence of increasing maturation rate. In addition, we notice that as the equilibrium of MmC increases due to the parameter increase, there is a direct relationship with the decrease in equilibrium of the ImC. This can be justified by the fact that the MmC cells directly reduces the number of ImC.

Let's now consider the parameter sweep of κ_1:

For the parameter sweep of κ_1 in figure 13, the equilibrium values of each state were calculated by taking the end values of each realization. Three realizations were ran in this simulation. Recall that the parameter κ_1 represents the rate of ImC in-flow. As our in-flow of ImC increases, the tumor equilibrium steadily decreases. The M_1 equilibrium seems to not fluctuate as we increase the parameter. However, we do notice that there is an increase in M_2 equilibrium. This can be justified by an increase in the maturation of ImC as there is an increase in the in-flow of ImC. The first two values of κ_1, along with all other parameter values, indicate an R_0 greater than one, which represents a tumor endemic equilibrium. The results of tumor equilibrium for these first two values of κ_1, show a correct approximated portrayal of the mean-field in comparison with the CA results. However, the last two values of κ_1, along with the all other parameters, indicate an R_0 value less than one, which represents a tumor free equilibrium. In this case, the R_0 value of the mean-field approximation does not correctly represent the results of the CA since we notice that there is still an endemic tumor equlibria. This can be due to the mean-fields inability to model the spatial effects of the system. It is worth noting that if we continue to continue to increase the parameter value of κ_1, the tumor will eventually die.

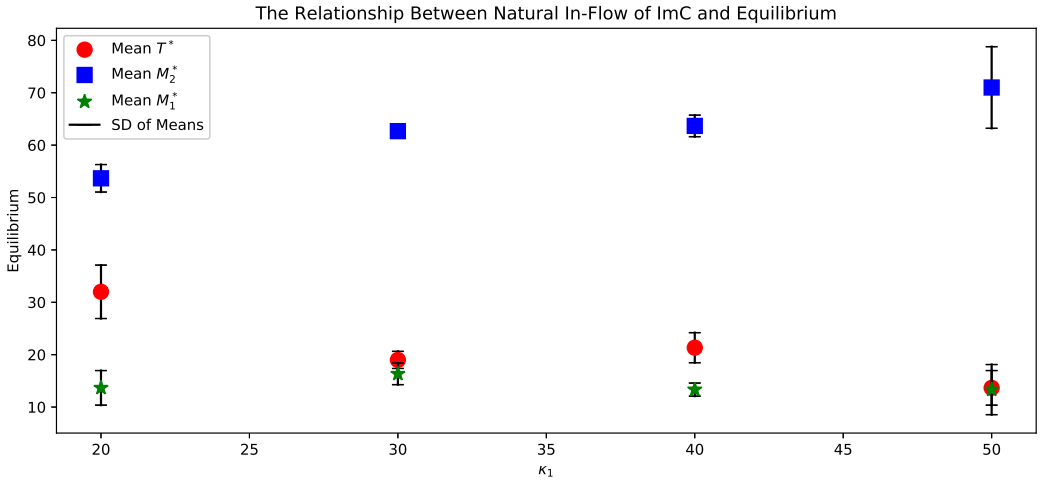

Figure (13) Parameter sweep on κ_1 with a range from 20 to 50, using 10 by 10 lattice size. Parameter Values: $\alpha = 100$, $\psi_1 = 0.02$, $\psi_2 = 0.02$, $\lambda = 0.432$, $\psi_T = 0.02$, $\beta = 0.00202$, $\kappa_2 = 10$, $g = 0.00125$, $b = \frac{n^2}{5}$, $\theta = 0.02$. Initial conditions: $T_0 = 20$, $M_{1,0} = 0$,$M_{2,0} = 0$. End Time = 500 days.

4.6 Stochastic Cellular Automaton vs Mean Field Approximation

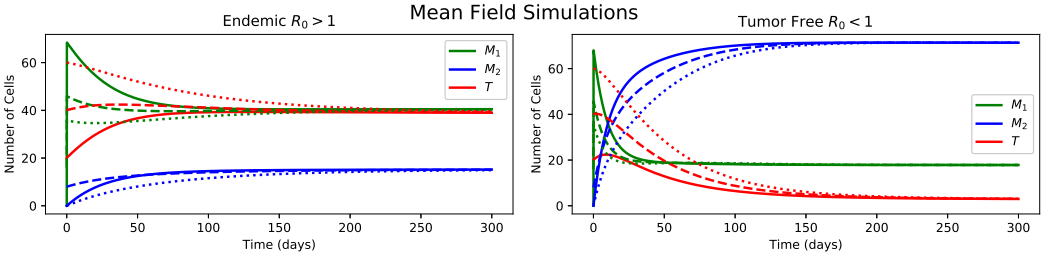

Figure (14) Mean-Field simulations considering parameters used in CA simulations of Figure 6, and 9. Left: Endemic tumor growth. Right: Tumor extinction (right).

On one hand, we notice similar behavior in figures 14 and 6 for a tumor endemic behavior with $R_0 = 7.17$ which means that the tumor free equilibria is unstable. The main difference between both models is given by the steady state of tumor cells where 80 stands for the CA model and 40 for the MF approximation. On the other hand, we can notice that both figures 14 and 9 represent tumor extinction behavior for the tumor steady state of each simulation. Analogously, we have that the steady state at t = 400 days is approximately $T^* = 20$ for the CA and $T^* = 0$ for the MF approximation. From both scenarios we can conclude that the MF approximation underestimates the R_0 for the tumor survival threshold in the CA.

5 Discussion

In this project, we studied the spatial dynamics of non-small cell adenocarcinoma at the initial stages in the epithelial tissue of an alveolus. A stochastic Cellular Automaton (CA) model was developed in the form of a continuous-time Markov chain to capture the local effects of tumor cells' defense mechanism (the secretion of cytokines that inhibit the maturation of immature myeloid cells). Each cell is in one of the following states: empty, immature myeloid cell, mature myeloid cell, or tumor. All transition events between one state variable to another are independent and the waiting time between each event is distributed exponentially. For this Poisson process, the states are given by a Markov chain where the state variables are distributed in a Von Neumann

neighborhood with toroidal boundary conditions. We noticed that the lattice size do not affect the steady state of tumor cells for the CA model as mentioned before in figure 5.

In addition, we considered the mean-field approximation of the stochastic Cellular Automaton through an ODE system to observe non-spatial interactions of immature myeloid cells, mature myeloid cells, and tumor cells from a deterministic perspective. The ODE system is defined by the difference between the in-flows and out-flows of each state. Through the mean-field approximation, we analyzed the local stability related with the tumor-free equilibrium of the system. In contrast to Cellular Automaton, this approximation allowed the analysis of global interactions instead of local interactions, assuming a well mixing between variables. In addition, we found a R_0 and addressed its meaning with regards to the tumor free equilibrium. We provided a simulation of the mean-field conditions that satisfy an $R_0 < 1$ and $R_0 > 1$ which describes a tumor extinction

The parameters used in Figure 7 and 8 for the Cellular Automaton simulations show that there exists a co-existence between mature myeloid cells and tumor cells. These suggest that despite the surpassing of mature myeloid cell quantity over tumor cell quantity, it is not sufficient for tumor eradication. The possibility of coexistence implies two things. First, despite the ability of mature myeloid cells to mass to a quantity greater than tumor cell numbers (Figure 9), the tumor cell population is able to adjust their defense mechanism and exploit space in such a way that allows them to survive and evade eradication. Second, despite tumor cells ability to mass to quantities greater than myeloid cell numbers (Figure 9), myeloid cells can still maintain a steady population count. This co-existence can be explained by tumor immunoediting phases: designed elimination, equilibrium, and escape [29]. The immune system tries to eradicate tumor cells from the body but is not always successful. This causes surviving tumor cells to evolve and proliferate [29, 23]. This cycle continues and surviving tumor cells continue to evolve. The tumor cells that evolve become better at evading the immune system, develop resistance to other physical attacks, and are more effective at suppressing anti-tumor immune responses which leads to the escape phase [29, 33]. In particular, tumor cells induce $CD11b_+Gr\text{-}1_+$ cells that suppress myeloid cells in order to evade the immune system [33].

We swept the most critical parameters related with the tumor growth (θ, β, λ, and κ_1) through CA simulations in order to look for critical behaviors of the system. We found a set of ranges to analyze for four parameters (θ, β, λ and κ_1) based on R_0 evaluations less than one and greater than one. This allowed for a comparison of the results between the mean-field approximation and the cellular automaton in which case there were various situations where the mean-field results (the evaluated R_0 based on parameter values simulated) did not relate to the results from the cellular automaton simulations. This ultimately allowed us to notice the limitation of the mean-field approximation in its inability to model the spatial dynamics of the system. We obtained three equilibrium points, one tumor free and at least one tumor endemic (See Figure 4). We obtained an expression for R_0 and performed simulations on tumor growth for $R_0 < 1$ and $1 < R_0$ at the tumor free-equilibrium in which case our tumor went to extinction and steady-state, respectively.

In Figure 14 we used the same parameter values for tumor endemic as in Figure 6 and for tumor extinction as in Figure 9. The results of Figure 14 underestimates the results of Figure 6 and 9. For instance, the results of the stochastic cellular automaton simulations of tumor endemic shows that the number of tumor cells is around 80, whereas the mean field simulations suggest that the number of tumor and immature myeloid cells are around 40. Similarly, for tumor extinction, the results of the stochastic cellular automaton shows that the number of mature myeloid cells is around 80, whereas in the mean field simulations the number of mature myeloid cells reach a boundary condition given by the total number of cells of the simulation.

Figure 6 represent cases of rapid tumor spread. The proportion of initial tumor cells with respect to the lattice size is $\frac{1}{5}$. After the first 50 days, tumor cells reach a boundary condition given by the lattice size. At this stage, the tumor cells are defined as carcinoma in situ, which is a group of tumor cells that are found on the same tissue where they arose [4]. However, due to the aggressive behavior of tumor spread it is possible for this clump of tumor cells to spread to invade main bronchus and visceral pleura [32]. The stage in which tumor cells overcome immune recognition and become clinically noticeable is also known as scape stage [6]. Moreover, tumor cells in the escape stage are able to secrete cytokines, as a defense mechanism, that leads to an enhanced tumor proliferation and metastasis [6]. Note that manipulating the rates of inhibition of maturation of immature myeloid cells by tumor cells (g), tumor death induced by mature myeloid cells (β), and maturation of immature myeloid cells (θ), we can obtain a change in the behavior of tumor cells and how they spread in the lattice. These findings could lead to the implementation of

new cancer immunotherapies that boost the activation of mature myeloid cells against tumor cells in order to halt tumor spread and metastasis. Several studies have shown that mature myeloid cells are able to recognize and present tumor cell-derived molecules to T-cells, which are responsible to kill tumor cells by the secretion of perforin [22, 14, 31, 5, 28].

A large number of mature myeloid cells can kill tumor cells and decrease the tumor population, as seen in Figure 9. Nowadays, mature myeloid cell-based immunotherapy is able to enhance the production of mature myeloid cells, thus increasing the number of tumor cells that are presented to T-cells for their elimination [11]. Furthermore, our stochastic Cellular Automaton model and Mean Field approximation confirms the potential efficacy of myeloid cell-based immunotherapies, as seen in Figure 12, increasing the value of θ from 0.01 to 0.04 affect the steady state of tumor cells and mature myeloid cells. This is, small values of θ promotes tumor endemic tumor spread, whereas high values of θ lead to an increase in the population of mature myeloid cells and tumor extinction despite the tumor defense mechanism. This result is also confirmed by our R_0 (See Figure 4).

6 Conclusions

The discrete space of our stochastic CA model enables us to study the spatial dynamics of cancer at the cell-to-cell interaction level. Other key aspects of our model are the inclusion of immature myeloid cells migration in response to tumor cells, the local effects of the defense mechanism of tumors against maturation of myeloid cells, and the empty space that a cell leaves after death. Nowadays, myeloid cell-based immunotherapies focus on raising the levels of mature myeloid cells which are able to kill and present tumor cells to T-cells, thus stimulating the immune system to fight tumor cells and halt tumor proliferation and metastasis. Our model enables researchers to study the three phases of immunoediting: elimination equilibrium and scape, and gain more insight about the complex interactions between the immune system and tumor cells at early stages of non-small cell adenocarcinoma.

7 Future Work

Despite the results of this project, more stochastic Cellular Automaton simulations with a bigger lattice size and for a greater number of days are needed in order to examine more effective cancer treatment strategies among practitioners and medical doctors in the field. Moreover, further analysis on the behavior of tumor cells and their interaction with the immune system would help researchers gain a deeper understanding about the mechanistic behavior of caner. In addition, similar simulations can be implemented to study the behavior of cell competition and its effects on the tissue.

For the mean-field approximation, we considered an expected value approximation of the number of TM_1 and TM_2 pairs. Future works can be done on finding the actual expected values of TM_1 and TM_2 pairs in order to best implement the mean-field approximation. Pair-approximations could also be considered in future work because they will allow more accurate approximations of the spatial dynamics for the system.

8 Acknowledgements

We would like to thank Dr. Carlos Castillo-Chavez, Founding and Co-Director of the Mathematical and Theoretical Biology Institute (MTBI), for giving us the opportunity to participate in this research program. We would also like to thank Co-Director Dr. Anuj Mubayi as well as Coordinator Ms. Rebecca Perlin and Management Intern Ms. Sabrina Avila for their efforts in planning and executing the day to day activities of MTBI. We also want to give special thanks to Dr. Christopher Kribs. This research was conducted as part of 2018 MTBI at the Simon A. Levin Mathematical, Computational and Modeling Sciences Center (MCMSC) at Arizona State University (ASU). This project has been partially supported by grants from the National Science Foundation (NSF – Grant MPS-DMS-1263374 and NSF – Grant DMS-1757968), the National Security Agency (NSA – Grant H98230-J8-1-0005), the Alfred P. Sloan Foundation, the Office of the President of ASU, and the Office of the Provost of ASU.

9 Appendix

9.1 R_0 Computation

In section 3.1, for the equation (28) consider the following computation in order to get (29):

$$
\begin{aligned}
R_0 &= \frac{\lambda\psi_2(4\theta+\kappa_2+\psi_1)}{4\beta\theta\kappa_1+4\theta\psi_T(\kappa_1+\psi_2)+\psi_2\psi_T(\kappa_1+\kappa_2+\psi_1)} \\
R_0 &= \frac{\lambda}{\frac{4\theta(\beta\kappa_1+(\kappa_1+\psi_2)\psi_T)+(\kappa_1+\kappa_2+\psi_1)\psi_2\psi_T}{\psi_2(4\theta+\kappa_2+\psi_1)}} \\
R_0 &= \frac{\lambda}{\frac{4\theta(\beta\kappa_1+\kappa_1\psi_T)+\kappa_1\psi_2\psi_T+(4\theta+\kappa_2+\psi_1)\psi_2\psi_T}{\psi_2(4\theta+\kappa_2+\psi_1)}} \\
R_0 &= \frac{\lambda}{\psi_T+\frac{\kappa_1(4\theta\beta+4\theta\psi_T+\psi_2\psi_T)}{\psi_2(4\theta+\kappa_2+\psi_1)}} \\
R_0 &= \frac{\lambda}{\psi_T+\frac{4\theta\beta\kappa_1}{\psi_2(4\theta+\kappa_2+\psi_1)}+\frac{4\theta\psi_T\kappa_1}{\psi_2(4\theta+\kappa_2+\psi_1)}+\frac{\kappa_1\psi_T}{4\theta+\kappa_2+\psi_1}} \\
R_0 &= \frac{\lambda}{\psi_T+\gamma\kappa_1(\frac{\beta+\psi_T}{\psi_2}+\frac{\psi_T}{4\theta})}
\end{aligned}
\tag{15}
$$

where

$$
\gamma = \frac{4\theta}{(4\theta+\kappa_2+\psi_1)}
$$

$$
\begin{aligned}
R_0 &= \frac{\lambda}{\psi_T+R_{M_2}(R_{M_1}(\beta+\psi_T+\frac{\psi_T}{R_{M_2}}))} \\
&= \frac{\lambda}{\psi_T(R_{M_1}+1)+R_{M_2}R_{M_1}(\beta+\psi_T)} \\
&= \frac{\lambda}{\psi_T(R_{M_1}+R_{M_2}R_{M_1}+1)+\beta R_{M_2}R_{M_1}} \\
&= \frac{\lambda}{\psi_T(R_{M_1}+R_{M_2}R_{M_1}+1)+\beta R_{M_2}R_{M_1}}
\end{aligned}
$$

where

$$
R_{M_1} = \frac{\kappa_1}{4\theta+\kappa_2+\psi_1}, R_{M_2} = \frac{4\theta}{\psi_2}
$$

9.2 Stochastic Realization: Clustered Tumor Initial Conditions

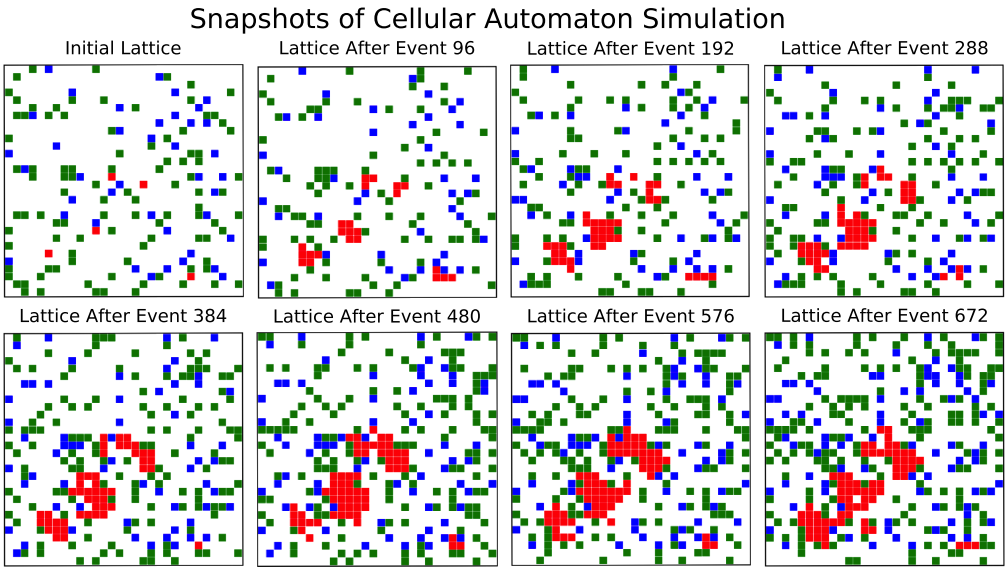

Figure (15) Sample stochastic CA simulation to visualize dynamics on the lattice.

References

[1] *How does the immune system work?* https://www.ncbi.nlm.nih.gov/pubmedhealth/PMH0072548/. Accessed: 2018-07-10.

[2] *Immune system*. https://www.ncbi.nlm.nih.gov/pubmedhealth/PMHT0025680/. Accessed: 2018-07-10.

[3] *Key statistics for lung cancer*. https://www.cancer.org/cancer/non-small-cell-lung-cancer/about/key-statistics.html. Accessed: 2018-07-10.

[4] *Nci dictionary of cancer terms*. https://www.cancer.gov/publications/dictionaries/cancer-terms/def/carcinoma-in-situ/. Accessed: 2018-07-20.

[5] B. Almand, J. I. Clark, E. Nikitina, J. van Beynen, N. R. English, S. C. Knight, D. P. Carbone, and D. I. Gabrilovich, *Increased production of immature myeloid cells in cancer patients: a mechanism of immunosuppression in cancer*, The Journal of Immunology, 166 (2001), pp. 678–689.

[6] V. K. Anagnostou and J. R. Brahmer, *Cancer immunotherapy: a future paradigm shift in the treatment of non–small cell lung cancer*, Clinical Cancer Research, 21 (2015), pp. 976–984.

[7] R. J. de Boer and P. Hogeweg, *Interactions between macrophages and t-lymphocytes: tumor sneaking through intrinsic to helper t cell dynamics*, Journal of theoretical biology, 120 (1986), pp. 331–351.

[8] L. G. de Pillis, W. Gu, and A. E. Radunskaya, *Mixed immunotherapy and chemotherapy of tumors: modeling, applications and biological interpretations*, Journal of theoretical biology, 238 (2006), pp. 841–862.

[9] A. Di Gregorio, S. Bowling, and T. A. Rodriguez, *Cell competition and its role in the regulation of cell fitness from development to cancer*, Developmental cell, 38 (2016), pp. 621–634.

[10] A. Diefenbach, E. R. Jensen, A. M. Jamieson, and D. H. Raulet, *Rae1 and h60 ligands of the nkg2d receptor stimulate tumour immunity*, Nature, 413 (2001), p. 165.

[11] D. Escors, *Tumour immunogenicity, antigen presentation, and immunological barriers in cancer immunotherapy*, New journal of science, 2014 (2014).

[12] O. Finn, *Immuno-oncology: understanding the function and dysfunction of the immune system in cancer*, Annals of oncology, 23 (2012), pp. viii6–viii9.

[13] O. J. Finn, *A believer's overview of cancer immunosurveillance and immunotherapy*, The Journal of Immunology, 200 (2018), pp. 385–391.

[14] D. I. Gabrilovich, S. Ostrand-Rosenberg, and V. Bronte, *Coordinated regulation of myeloid cells by tumours*, Nature Reviews Immunology, 12 (2012), p. 253.

[15] S. I. Grivennikov, F. R. Greten, and M. Karin, *Immunity, inflammation, and cancer*, Cell, 140 (2010), pp. 883 – 899.

[16] W. J. Grossman, J. W. Verbsky, W. Barchet, M. Colonna, J. P. Atkinson, and T. J. Ley, *Human t regulatory cells can use the perforin pathway to cause autologous target cell death*, Immunity, 21 (2004), pp. 589–601.

[17] D. Hanahan and R. A. Weinberg, *Hallmarks of cancer: The next generation*, Cell, 144 (2011), pp. 646 – 674.

[18] J. M. Hanna and M. W. Onaitis, *Cell of origin of lung cancer*, Journal of carcinogenesis, 12 (2013).

[19] M. A. Hayat, *Methods of Cancer Diagnosis, Therapy and Prognosis: General Methods and Overviews, Lung Carcinoma and Prostate Carcinoma*, vol. 2, Springer Science & Business Media, 2008.

[20] N. C. Institute, *What is cancer?* https://www.cancer.gov/about-cancer/understanding/what-is-cancer. Accessed: 2018-07-10.

[21] W. J. Janssen, D. L. Bratton, C. V. Jakubzick, and P. M. Henson, *Myeloid cell turnover and clearance*, Microbiology spectrum, 4 (2016).

[22] I. Kareva, F. Berezovskaya, and C. Castillo-Chavez, *Myeloid cells in tumour–immune interactions*, Journal of biological dynamics, 4 (2010), pp. 315–327.

[23] C. M. Koebel, W. Vermi, J. B. Swann, N. Zerafa, S. J. Rodig, L. J. Old, M. J. Smyth, and R. D. Schreiber, *Adaptive immunity maintains occult cancer in an equilibrium state.*, Nature, 450 (2007), pp. 903 – 907.

[24] V. Labi and M. Erlacher, *How cell death shapes cancer*, Cell death & disease, 6 (2016), p. e1675.

[25] A. Lanzavecchia and F. Sallusto, *Dynamics of t lymphocyte responses: intermediates, effectors, and memory cells*, Science, 290 (2000), pp. 92–97.

[26] J. C. Liu and J. A. Ridge, *Chapter 67 - what is cancer?*, in Abernathy's Surgical Secrets (Seventh Edition), A. H. Harken and E. E. Moore, eds., Elsevier, seventh edition ed., 2018, pp. 307 – 310.

[27] N. Margolus and T. Tommaso, *Cellular Automata Machines: A New Environment for Modeling*, MIT Press Cambridge, MA, USA ©1987, 1987.

[28] D. Marvel and D. I. Gabrilovich, *Myeloid-derived suppressor cells in the tumor microenvironment: expect the unexpected*, The Journal of clinical investigation, 125 (2015), pp. 3356–3364.

[29] K. Movahedi, M. Guilliams, J. Van den Bossche, R. Van den Bergh, C. Gysemans, A. Beschin, P. De Baetselier, and J. A. Van Ginderachter, *Identification of discrete tumor-induced myeloid-derived suppressor cell subpopulations with distinct t cell–suppressive activity*, Blood, 111 (2008), pp. 4233–4244.

[30] K. Murphy and C. Weaver, *Janeway's immunobiology*, Garland Science, 2016.

[31] P. Oberoi, R. A. Jabulowsky, H. Bähr-Mahmud, and W. S. Wels, *Egfr-targeted granzyme b expressed in nk cells enhances natural cytotoxicity and mediates specific killing of tumor cells*, PLoS One, 8 (2013), p. e61267.

[32] M. Reck, S. Popat, N. Reinmuth, D. De Ruysscher, K. Kerr, and S. Peters, *Metastatic non-small-cell lung cancer (nsclc): Esmo clinical practice guidelines for diagnosis, treatment and follow-up*, Annals of oncology, 25 (2014), pp. iii27–iii39.

[33] J. B. Swann and M. J. Smyth, *Immune surveillance of tumors*, The Journal of clinical investigation, 117 (2007), pp. 1137–1146.

[34] P. Van den Driessche and J. Watmough, *Reproduction numbers and sub-threshold endemic equilibria for compartmental models of disease transmission*, Mathematical biosciences, 180 (2002), pp. 29–48.

[35] J. E. Visvader, *Cells of origin in cancer*, Nature, 469 (2011), p. 314.

The Effect of Gonadotropin-Releasing Hormone (GnRH) on the Regulation of Hormones in the Menstrual Cycle: A Mathematical Model

Shanell S. George[1], Laura O. Mora Mercado[2], Corina Y. Oroz[3], Darwin X. Tallana-Chimarro[4], Juan R. Melendez-Alvarez[5], Anarina L. Murrillo[6], Carlos W. Castillo-Garsow[7] and Karen R. Ríos-Soto[2]

[1]Lehman College, The City University of New York, Bronx, NY
[2]University of Puerto Rico, Mayagüez, PR
[3]Pomona College, Claremont, CA
[4]Yachay Tech University, Urcuquí, Ecuador
[5]Arizona State University, Tempe, AZ
[6]University of Alabama at Birmingham, Birmingham, AL
[7]Eastern Washington University, Cheney, WA

Abstract

Gonadotropin Releasing Hormone (GnRH) is the drving force for hormonal regulation during the menstrual cycle. $GnRH$ signals the anterior pituitary gland to secrete follicle stimulating hormone (FSH) and luteinizing hormone (LH) which promotes the release of estradiol (E_2) and progesterone (P_4). Interferences in the cyclic interactions have been shown to cause irregularities in the menstrual cycle. In this study, the non-linear dynamics of $GnRH$, FSH, LH, E_2, and P_4 are examined. A simplified model of six non-linear ordinary differential equations is developed to model the effect of $GnRH$ on the dynamics of hormones in the menstrual cycle. A mathematical analysis is performed to observe the regulation of $GnRH$ in a monthly cycle. Our findings suggest that the relationship between E_2 and $GnRH$ plays an important role in concentrations and patterns of release of the hormones involved in the menstrual cycle.

1 Introduction

Understanding the structural mechanisms of the female menstrual cycle is necessary to gain a better understanding of the female reproductive system and conditions that may affect it. This is critical given that roughly 50.5% of the U.S. population is female [2]. The menstrual cycle is defined as the hormonal regulation of three stages: follicular phase, ovulation, and luteal phase. The menstrual cycle is regulated by the endocrine system through a series of feedback mechanisms and hormonal interactions. The functional process of the menstrual cycle is initiated by the secretion of gonadotropin under the influence of $GnRH$. The signaling processes between the hypothalamus, pituitary, and ovaries (also referred to as the hypothalamic-pituitary-ovarian axis) are critical for the regulation and maintenance of a normal cycle. On average, the menstrual cycle should occur 21 to 35 days [1, 4]. However, any physiological factors can alter the length of the cycle causing extreme variability.

External and internal pressures can alter the length of the cycle causing extreme variability. One of these abnormalities is the functional hypothalamalic amenorhera (FHA), which is the absence of menstruation for a period of three months or greater due to a perturbance in the signaling of gonadotropin releasing hormone ($GnRH$) [6]. A regulated pulse rate of $GnRH$ to the hypothalamus is vital to the signaling process that begins the secretion of follicle stimulating hormone (FSH) and luteinizing hormone (LH). By understanding the signaling processes and the behavior of these hormones in the menstrual cycle, we develop a mathematical model that captures the dynamical interactions between $GnRH$, FSH, LH, E_2, and P_4. As a result, we gain further understanding as to how disturbances in the production and regulation of $GnRH$ can cause irregularities in the menstrual cycle and to what extent.

In recent years, studies have attempted to mathematically model the menstrual cycle in order to capture the physiological phenomena of the signaling behavior that occur. In 2009, Isabel Reinecke *etal*., used a system of delay differential equation to model the menstrual cycle with the purpose of modeling feedback mechanism in the signaling process, including a GnRH pulse generator [9]. A simpler model consisting of a system of three nonlinear delay differential equations was developed in order to describe the hormonal interactions along the HPOA that can later be extended to future models involving the disruption of the menstrual cycle [7]. Another approach was developed by Brueggemanns model with the aim to predict potential fertility windows. Brueggemann constructed a simple model with four differential equations, taking period length as an input parameter without including $GnRH$, with the intent to simulate a complex system [10, 5]. However, in this project we construct a reduced model that can study the effect of $GnRH$ on the cycle without accounting for time delays while still demonstrating the hormonal interactions and feedback mechanisms occurring in the menstrual cycle.

1.1 Hypothalamic-Pituitary-Ovarian Axis

The hypothalamic-pituitary-ovarian axis is orchestrated by a series of hormones that work in concert to regulate the function of the menstrual cycle. In the female reproductive system, the hypothalamus releases gonadotropin releasing hormone, GnRH, at high levels, which travels through the anterior pituitary circulating blood stimulating cells called the gonadotrophes. Gonadotrophes are responsible for the productions and release of follicular stimulating hormone (FSH) and lutenizing hormone(LH). FSH and LH travels to the ovaries through the bloodstream where they aid in the maturation of the premordial follicles into fully mature follicle, this process is known as the follicular phase. The growth of the follicles is important because it contains the immature egg that will develop over time until release from the follicles. As the follicle matures estradiol, active form of estrogen during the menstrual cycle, is released. In the present of low estradiol levels FSH will increase and LH will stay at a steady state given that GnRH is still increasing and releasing FSH and LH. As estradiol increases, FSH will decrease and LH levels will begin to increase. The follicular phase usually last around 14 days. Approaching day 14 an increase in LH will occur transitioning from follicular phase into the ovulatory phase.

During the ovulatory phase, the increase in LH causes the mature follicle to release an egg. The egg will travel through the fallopian tubes awaiting fertilization. The ovulatory phase is quiet short. Following the ovulatory phase, the luteal phase will begin will the degration of the corpus luteum. The corpus luteum is the structure that remains after the follicle has released the matured egg. As the corpus luteum begins to degrade it releases progesterone and other inhibitory hormones, such as Inhibin, to slow the production of hormones, such as GnRH, FSH, LH, and E_2, and the maturation of new follicles. As the corpus luteum degrades and fertilization has not occurred progesterone

levels will decrease. In result, menstruation will occur causing the uterine line to shed. Finally once the discharge of the lining has discontinued the body will prepare itself for the next cycle.

In this study, we aim to construct a simplified model that captures the qualitative behavior of the menstrual cycle in order to study the behaviors that GnRH will have on the system as parameters vary. This study is arranged in the following sections. In Section 2, we divided the hypothalumus-pititary-ovarian axis into five compartments: GnRH, FSH, LH, E_2 and P_4 to describe the regulatory mechanisms each hormone have on one another. Following this, we constructed a system of six non-linear differential equations (basic model) that simplifies the regulatory pathway of the menstrual cycle as seen in Section 2.2. In Section 2.3 we extend our model by developing an entirely new equation for GnRH, called GnRH(t) providing us a new model (sinusoidal model) where GnRH(t) replaces the GnRH ordinary non-linear differential equation. In Section 3, we perform numerical simulations on both the basic model and the sinusoidal model, following a hopf bifurcation analysis performed using the basic model. In Section 4, we perform a sensitivity analysis using model 1 to understand how parameters in GnRH in model consisting of the six non-linear ordinary differential effect the concentration of the hormones in the system. Lastly, we summarize our study in Section 5.

2 Methodology

2.1 Model Description

To capture the dynamic of the menstrual cycle mathematically, a system of six non-linear ordinary differential equations were decomposed from two independent studies. The equations developed simplifies the dynamic of the menstrual cycle to explore the effects of hormonal disruptions by GnRH. Each equation captures the qualitative behavior of the hormones, in which they are defined as concentration per day. In order to describe the feedback regulation between the hormones of our model we use Hill functions, which characterize inhibition and/or stimulation of hormones production. A description of the equations are illustrated by the model in Figure 2. The change in concentration of the hormones GnRH, LH, FSH, E_2 and P_4 are reflected in 4a, 4b, 4c, 4d and 4e, respectively. Additionally, this model proposes Equation 4f as a tool that accounts for the transition of the follicular stage to the corpus luteum, in addition to the changes in progesterone precursor levels.

2.1.1 Hill Function

Hill Functions are used in this study to model and understand the feedback mechanism of the hypothalamic-pituitary-ovarian axis model mathematically [9]. Feedback mechanism alters the rate at which the production of a hormone is being inhibited or stimulated. Generally, hormonal output is mediated by either *positive feedback* or *negative feedback*. Positive feedback mechanism tend to stimulate the release of a hormone while, negative feedback mechanism tend to down-regulate the release of a hormone.

Positive feedback is defined in Equation 1 given by:

$$h^+(S, T_1, n) := \frac{[S]^n}{T_1^n + [S]^n} \tag{1}$$

While negative feedback is defined in Equation 2 given by:

$$h^{-}(S, T_2, n) \quad := \quad \frac{T_2^n}{T_2^n + [S]^n} \tag{2}$$

where T_1 and $T_2 \in \mathbb{R}_+$ represent the threshold values that the hormonal concentration must surpass in order to be efficient for up-regulation or down-regulation, respectively. The threshold value signifies the half-way point at which the feedback mechanism is either close to being efficient or ineffective. Ultimately, as more stimulation or inhibition occurs the Hill function will exhibit values either close to 1 or 0, respectively, as seen in Figure 1 [9]. The concentration of the hormone is denoted by S, which acts in concert with the feedback mechanism [9] and $n > 1$ represents the steepness of the graphs; the steeper the graph, the faster the reaction; while the less steep the graph is, the slower the reaction. Moreover, S represents the concentration of the hormone producing the feedback (Fig 1a and 1b). For instance, to describe the positive feedback between hormone L induced by hormone S, a differential equation is derived to study the changes of L with respect to time and Equation 1 as follows, for some parameter C_1.When the concentration of S is bigger than the threshold value T_1, then there is a stimulation of production:

$$\frac{dL}{dt} = S, C_1 h^{+}(S, T, n)$$

On the other hand, negative feedback between hormone L induced by hormone S is given by,

$$\frac{dL}{dt} = C_2 h^{-}(S, T, n),$$

which models the inhibition of production of hormone L due to hormone S [9].

Moreover, production of hormone L can be stimulated or inhibited depending on the concentration of hormone S. This behavior can be described using a biphase Hill function given by,

$$h^{-,+}(S) = h^{+}(S, T_1, n) + h^{-}(S, T_2, n) \tag{3}$$

provided that $T_1 > T_2$ to model the dynamics of inhibition and stimulation of hormone S on hormone L. In this case, for concentrations of S less than $(T_1 \cdot T_2)^{1/2}$ L is inhibited (Fig 1c); and for higher concentrations than $(T_1 \cdot T_2)^{1/2}$, hormone S stimulates L [9].

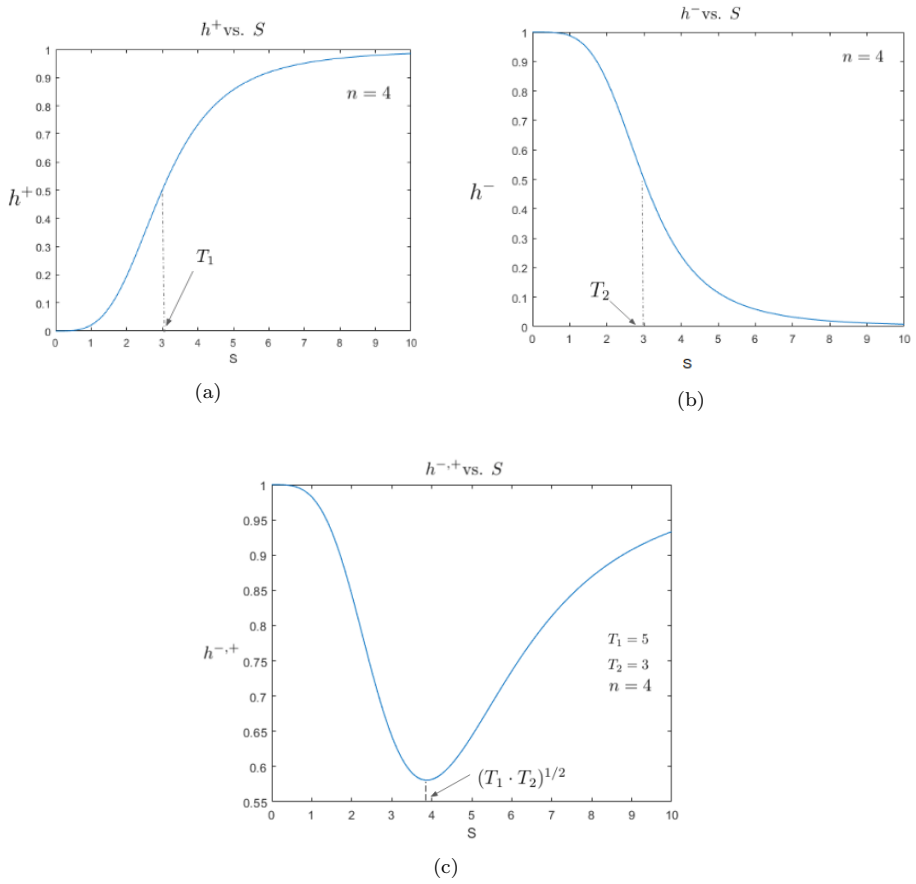

Figure 1: Hill functions: (a) represents the positive Hill function, Equation 1, which models stimulation for concentrations of S bigger than the threshold value T_1. (b) represents the negative Hill function, Equation 2, which models inhibition for concentrations of S bigger than the threshold value T_2. (c) represents the biphase Hill function, Equation 3 which models positive feedback and negative feedback depending on the concentrations of S.

2.2 System of Ordinary Differential Equations

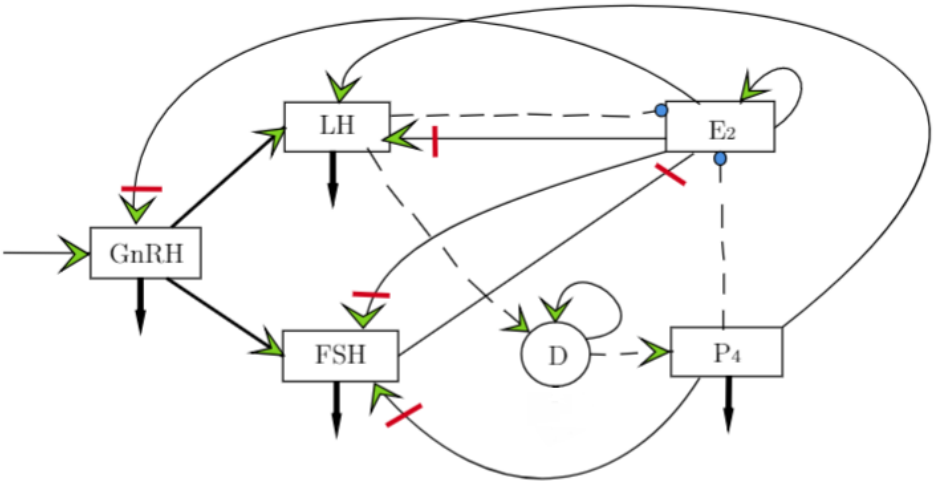

Figure 2: Mathematical Model describing the interaction of hormones in the menstrual cycle. Activation is represented by the solid line arrow heads. Bipashic interaction is represented by the solid line arrow with a stroke. Activation of degradation is represented by dashed lines with dot end. Promotion of production is represented by dashed arrow head. Full block arrows represent natural degradation of the hormone.

The system of equations corresponding to the model is as follows:

$$\frac{dGnRH}{dt} = C_1 + C_2\left(\frac{r_1^{n_1}}{r_1^{n_1}+E_2^{n_1}} + \frac{E_2^{n_2}}{q_1^{n_2}+E_2^{n_2}}\right) - \mu_1 GnRH \tag{4a}$$

$$\frac{dLH}{dt} = C_3\left(\frac{r_2^{n_3}}{r_2^{n_3}+E_2^{n_3}} + \frac{E_2^{n_4}}{q_2^{n_4}+E_2^{n_4}}\right)\cdot\frac{P_4^{n_5}}{q_3^{n_5}+P_4^{n_5}}\cdot GnRH - \mu_2 LH \tag{4b}$$

$$\begin{aligned}\frac{dFSH}{dt} = {} & C_4\left(\frac{P_4^{n_6}}{q_4^{n_6}+P_4^{n_6}}\cdot\frac{r_3^{n_7}}{r_3^{n_7}+(\alpha E_2+\beta P_4+ih0)^{n_7}}\right) \\ & \left[\left(\frac{r_4^{n_8}}{r_4^{n_8}+E_2^{n_8}} + \frac{E_2^{n_9}}{q_5^{n_9}+E_2^{n_9}}\right)GnRH\right] - \mu_3 FSH\end{aligned} \tag{4c}$$

$$\frac{dE_2}{dt} = C_5\cdot\frac{r_5^{n_{10}}}{r_5^{n_{10}}+FSH^{n_{10}}} - C_6\cdot E_2\cdot\frac{LH^{n_{11}}}{q_6^{n_{11}}+LH^{n_{11}}} + C_7\cdot\frac{E_2^{n_{12}}}{q_7^{n_{12}}+E_2^{n_{12}}} - C_8\cdot E_2\cdot\frac{P_4^{n_{13}}}{q_8^{n_{13}}+P_4^{n_{13}}} \tag{4d}$$

$$\frac{dP_4}{dt} = C_9 D - \mu_4 P_4 \tag{4e}$$

$$\frac{dD}{dt} = C_{10}\cdot\frac{r_6^{n_{14}}}{r_6^{n_{14}}+D^{n_{14}}}\cdot LH\cdot D - C_{11}\cdot\frac{D^{n_{15}}}{q_9^{n_{15}}+D^{n_{15}}} \tag{4f}$$

In order to use Hill functions to model the inhibitor/stimulator behavior of these hormones, we consider $q_1 > r_1$, $q_2 > r_2$ and $q_5 > r_4$. The change of $GnRH$ over time, Equation 4a, depends on E_2 and $GnRH$ itself. In this equation, C_1 represents the basal release rate per day of $GnRH$. The dependence of $GnRH$ on E_2 is given by a biphase Hill function, which shows that for concentrations less than $(r_1 \cdot q_1)^{1/2}$ E_2 acts as an inhibitor and for concentrations greater than this threshold as a stimulator. Additionally, $GnRH$ naturally degrades through metabolism at a rate per day μ_1. This parameter μ_1 also represents the portion of $GnRH$ that is not used for the menstrual cycle.

Equation 4b models the rate of change of LH that is dependent on E_2, P_4 and $GnRH$ at rate of C_3 per day. The first term shows that $GnRH$ concentration is necessary for growth of LH concentrations, whereas E_2 stimulates or inhibits LH depending on the threshold concentration value of the biphase function and on q_2. Moreover, for levels of P_4 greater than q_3 we have stimulation of LH production. LH naturally degrades and is metabolized at a rate μ_2.

The change in FSH over time, Equation 4c, depends on P_4, E_2, $GnRH$, and FSH. In the first term, $GnRH$ concentration is necessary for growth of FSH concentrations. This growth is given at rate of C_4 per day. If the levels of P_4 are greater than q_4 there is stimulation or production of FSH. Whether or not E_2 stimulate or inhibit the production and release of FSH depends on threshold concentration values r_4 and q_5. In addition, $\alpha P_4 + \beta E_2$ capture the dynamic of the hormone inhibin that is released during the luteal stage. The production of FSH is inhibited when $\alpha P_4 + \beta E_2 < r_3$. Parameter estimation of α and β was calculated in MATLAB using least square.

The change in concentration of E_2 over time, Equation 4d, depends on FSH, LH, E_2 and P_4. FSH inhibits E_2 at a rate C_5 and for concentrations larger than r_5. On the other hand, E_2 stimulates its own production for larger concentrations than q_7 and at a daily rate of C_7. Moreover, the second term shows that E_2 decreases its own production depending on the feedback of LH. When the levels of LH passes the threshold level q_6, E_2 signals the decrease in production of itself, i.e. inhibition occurs. The impact of this feedback depends on the constant daily rate of C_6 . For levels of P_4 greater than q_8 there is a decreasing in the rate of change of E_2 that depends on the concentration of E_2 and also on the constant of C_8 per day.

Equation 4e represents the rate of change of P_4, which has degradation rate μ_4, and increases as its precursor D increases, which occurs at a rate per day C_9. Finally, Equation 4f works as a precursor to P_4 in order to account for the follicular stages without including a time precursor in the dynamics of P_4. This precursor depends on the levels of LH and on its own values. LH is necessary for the growth of the precursor D, and for larger values of the precursor D the rate of change of D slows down.

Table 1 define the state variables of the model. While Table 2 provides a comprehensive description of the parameter values of the model described as well as their definitions.

Table 1: State variables of the system of ordinary differential equations

State Variables	Definition	Unit
GnRH	Gonadotropin Release Hormone	$\frac{\mu g}{L}$
LH	Luteinizing Hormone	$\frac{\mu g}{L}$
FSH	Follicular Stimulating Hormone	$\frac{\mu g}{L}$
E2	Estradiol	$\frac{ng}{L}$
P4	Progesterone	$\frac{nmol}{L}$
D	Precursor	$\frac{nmol}{L}$

Table 2: Parameters of the system of ordinary differential equations

No.	PARAM	Description	Units
1	C_1	basal release rate of $GnRH$	$\frac{\mu g}{d}$
2	C_2	conversion factor of $GnRH$ w.r.t the concentration of E_2	$\frac{\mu g}{d}$
3	C_3	conversion factor of LH w.r.t the concentration of E_2	$\frac{1}{d}$
4	C_4	conversion factor of FSH w.r.t the concentration of P_4, E_2 & $GnRH$	$\frac{1}{d}$
5	C_5	conversion factor of E_2 w.r.t the concentration of FSH	$\frac{ng/L}{d}$
6	C_6	conversion factor of E_2 w.r.t the concentration of LH and E_2	$\frac{1}{d}$
7	C_7	conversion factor of E_2 w.r.t the concentration of E_2	$\frac{ng/L}{d}$
8	C_8	conversion factor of E_2 w.r.t the concentration of FSH	$\frac{1}{d}$
9	C_9	conversion factor of P_4 w.r.t its delay, D	$\frac{1}{d}$
10	C_{10}	conversion factor of D w.r.t D and LH	$\frac{L}{\mu g * d}$
11	C_{11}	conversion factor of D w.r.t D	$\frac{nmol/L}{d}$
12	n_1	speed of inhibition of $GnRH$ dependent on E_2	unitless
13	n_2	speed of stimulation of $GnRH$ dependent on E_2	unitless
14	n_3	speed of inhibition of LH dependent on E_2	unitless
15	n_4	speed of stimulation of LH dependent on E_2	unitless
16	n_5	speed of stimulation of LH dependent on P_4	unitless
17	n_6	speed of stimulation of FSH dependent on P_4	unitless
18	n_7	speed of inhibition of FSH dependent on E_2 and P_4	unitless
19	n_8	speed of inhibition of FSH dependent on E_2	unitless
20	n_9	speed of stimulation of FSH dependent on E_2	unitless
21	n_{10}	speed of inhibition of E_2 dependent on FSH	unitless
22	n_{11}	speed of stimulation of E_2 dependent on LH	unitless
23	n_{12}	speed of stimulation of E_2 dependent on E_2	unitless
24	n_{13}	speed of stimulation of E_2 dependent on P_4	unitless
25	n_{14}	speed of inhibition of D dependent on D	unitless
26	n_{15}	speed of stimulation of D dependent on D	unitless
27	q_1	threshold value of E_2 that stimulates $GnRH$	$\frac{ng}{L}$
28	q_2	threshold value of E_2 that stimulates LH	$\frac{ng}{L}$
29	q_3	threshold value of P_4 that stimulates LH	$\frac{nmol}{L}$
30	q_4	threshold value of P_4 that stimulates FSH	$\frac{U}{L}$
31	q_5	threshold value of E_2 that stimulates FSH	$\frac{ng}{L}$
32	q_6	threshold value of LH that stimulates E_2	$\frac{\mu g}{L}$
33	q_7	threshold value of E_2 that stimulates E_2	$\frac{ng}{L}$
34	q_8	threshold value of P_4 that stimulates E_2	$\frac{nmol}{L}$
35	q_9	threshold value of D that stimulates D	$\frac{nmol}{L}$
36	r_1	threshold value of E_2 that inhibits $GnRH$	$\frac{ng}{L}$
37	r_2	threshold value of E_2 that inhibits LH	$\frac{ng}{L}$
38	r_3	threshold value of E_2 and P_4 that inhibits FSH	$\frac{nmol}{L}$
39	r_4	threshold value of E_2 that inhibits FSH	$\frac{ng}{L}$
40	r_5	threshold value of FSH that inhibits E_2	$\frac{\mu g}{L}$
41	r_6	threshold value of D that inhibits D	$\frac{nmol}{L}$
42	α	linear coefficient for E_2	$\frac{U}{ng}$
43	β	linear coefficient for P_4	$\frac{U}{nmol}$
44	μ_1	natural degradation rate of $GnRH$	$\frac{1}{d}$
45	μ_2	natural degradation rate of LH	$\frac{1}{d}$
46	μ_3	natural degradation rate of FSH	$\frac{1}{d}$
47	μ_4	natural degradation rate of E_2	$\frac{1}{d}$

2.3 Sinusoidal Equation for GnRH

$GnRH$ secretion acts on the anterior pituitary to regulate the production and release of LH and FSH, which ultimately triggers the cyclic reaction of the menstrual cycle. Findings have characterized that GnRH function is expressed through a series of pulsatile secretions.If the pulsatile release of GnRH increases, its levels in the body are higher. The higher levels of GnRH can be correlated with the width of GnRH curve: as the

concentration of GnRH increases, its width increases, and viceversa. For this reason, this study focused on the impact of width of GnRH. Through this analysis, we can determine a quantifiable impact of GnRH on LH and FSH, which ultimately control the transition between follicular phase, ovulation, and lutheal phase . For this purpose, the following equation was modified from [5] to capture the periodicity of GnRH pulse behavior:

$$GnRH(t) = g_1 + g_2 \cdot \exp\left(-g_3 \cdot \sin\left(\left(\pi \cdot \frac{t}{28}\right) + g_4\right)^2\right) \tag{5}$$

given g_1, g_2, g_3, g_4 positive parameters. The basal concentration of $GnRH$ is represented by the value of g_1. The amplitude of the $GnRH$ curve is represented by g_2, at which the time $GnRH$ reaches its peak along the interval is given by the value of g_4. The width of the curve of $GnRH$ depends only on the value of g_3. If g_3 increases, the width of the curve decreases, corresponding to less pulsatile release of GnRH. In contrast, for small values of g_3, the width is larger, which represents more pulsatile release of GnRH (see Table 3).

Equation 5 was used together with Equations 4b to 4f to get a different modeling approach to study the pulse behavior in our original system of equations. Then, we created a $MATLAB$ code to find numerical solutions for the second model. These results were used to calculate the width, maximum peak, and time at which the peak occurs for LH and FSH concentration curves (see Section 3.3).

Table 3: Parameters of GnRH(t) given by Equation 5.

Parameter	Description	Units
g_1	Basal concentration of GnRH(t)	$\frac{\mu g}{L}$
g_2	Amplitude of GnRH(t)	$\frac{\mu g}{L}$
g_3	Width Parameter	unitless
g_4	Phase Parameter	unitless

3 Analysis

In this section we seek qualitative results on what effect $GnRH$ has on LH and FSH. This can be achieved using system 4 by studying the occurrences of the system of hormonal regulation as $GnRH$ is changed.

3.1 Description of Data and Parameter Estimation

First we start with the estimation of baseline parameter values used on our model. The parameters used during analysis were obtained from two sources. In both Reinecke's and Brueggemann's models of the menstrual cycle, nonlinear least square approaches were used to estimate parameters [9, 5]. In the GynCycle model, Reinecke uses four different sources for experimental data with sample sizes ranging between 6 to 33 healthy women between all within the ages of 18 and 40 and with average cycles [9].

For the differential equations of $GnRH, LH$, and FSH, parameter values from Reinecke's model were used. For the differential equations of E_2, P_4, and D, parameter values of Brueggemann's model were considered. Together these values were used as a baseline of parameter values for the model, see Table 5 in A.1

Table 4: Estimated initial values of the state variables of the system of ordinary differential equations that produce periodic pulses.

State Variables	Definition	Value	Unit
GnRH	Gonadotropin Release Hormone	1.000	$\frac{\mu g}{L}$
LH	Luteinizing Hormone	25.34	$\frac{\mu g}{L}$
FSH	Follicular Stimulating Hormone	142.5	$\frac{\mu g}{L}$
E2	Estradiol	16.387	$\frac{ng}{L}$
P4	Progesterone	1.200	$\frac{nmol}{L}$
D	Precursor	1.000	$\frac{nmol}{L}$

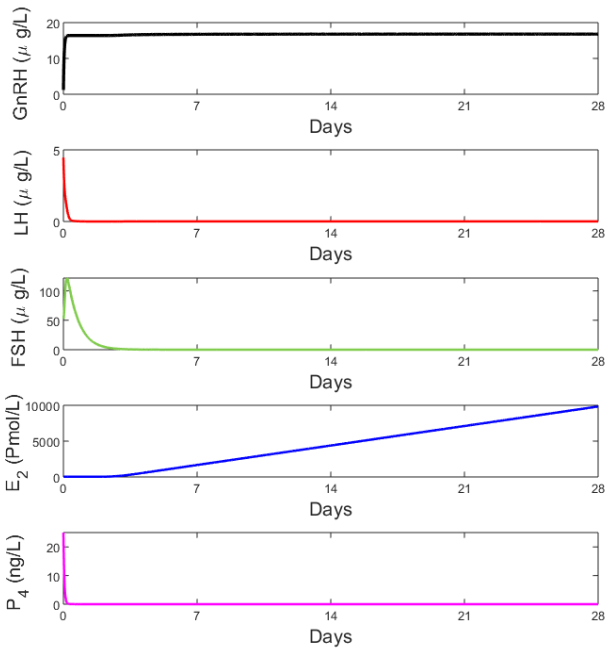

Figure 3: Numerical Simulation of the concentration of hormones as a function of time in our model with baseline parameter values as shown in Table 5.

Figure3 shows the concentration of hormones as a function of time for one menstrual cycle. Since the parameter values used were taken from more complicated models, this simulation does not resemble what happens during a normal cycle. Thus we modified baseline values to obtain a numerical stimulation that more closely resembled the patterns we know to be true of hormonal regulation in an average menstrual cycle [8]. These parameter values were then used for the rest of our work as the basis of our analysis. Many of the key components of the menstrual cycle are described in a reduced model of a complex dynamical system, however it comes at the expense of having less quantitative results.

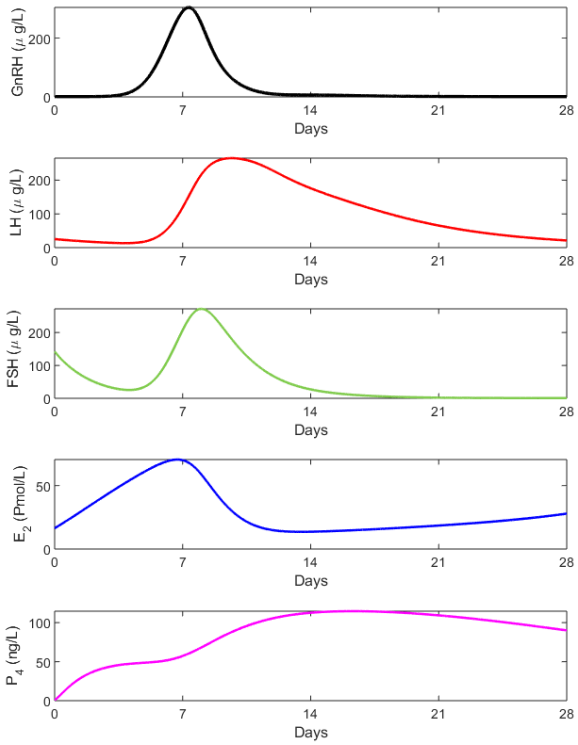

Figure 4: Representation of changes in hormonal concentration over a 28 day menstrual cycle using the parameter values from Table 6 using initial conditions provided in Table 4 above.

With a vector of initial conditions at t(0), the simulation in Figure 4 shows that at as $t(0) \rightarrow t(1) =$ day 1, E_2 and P_4 increase followed by the increase of $GnRH$. FSH starting at t_0 decreases, meanwhile $GnRH$ begins to increase, followed by the increase of FSH and LH. In a normal cycle, a peak of LH and FSH around day 14, when ovulation occurs. However, in Figure 4 FSH peaks around day 8. Although the simulation is not quantitatively accurate, the behavior of the system qualitatively coincides with what is known to occur during an average menstrual cycle such that E_2 activates $GnRH$ and $GnRH$ stimulates the release of LH and FSH [8].

3.2 Numerical Simulations of 6 Ordinary Differential Equation Model

In this section we show simulations of our model in order to demonstrate the minimum value at which stimulation and inhibition occur for $GnRH$ and for what values threshold parameters must be in order to have periodicity within a cycle.

3.2.1 Minimum concentration for stimulation

By definition of the Hill Function we know that in a biphase Hill function (Equation 3),$\sqrt{T_1 \cdot T_2}$ is the minimum concentration of the S hormone for stimulation [9].
First let $q_1 > r_1$, that is the threshold value of stimulation of $GnRH$ by E_2 is greater than the threshold condition of $GnRH$, also by E_2. The minimum value of the Hill function

$\frac{r_1^{n_1}}{r_1^{n_1}+E_2^{n_1}} + \frac{E_2^{n_2}}{q_1^{n_2}+E_2^{n_2}}$ with $n_1 = n_2 = 1$ is $E_2^{min} = \sqrt{q_1 \cdot r_1}$. In a plot of concentration of E_2 over time, there are two intersection points, t_1^{min} and t_2^{max}, for valus of E_2 as $E_2^{min} = \sqrt{q_1 \cdot r_1}$. That point separates the determinants of stimulation vs inhibition in $\frac{r_1^{n_1}}{r_1^{n_1}+E_2^{n_1}} + \frac{E_2^{n_2}}{q_1^{n_2}+E_2^{n_2}}$.

For example, when $q_1 = 75$ and $r_1 = 8$, $\sqrt{q_1 \cdot r_1} = 24.4949$. Observe that t_1^{min} is approximately around day 1 and t_2^{max} is approximately around day 10. As expected, for values of t in $[t_1^{min}, t_2^{max}]$ stimulation of $GnRH$ primary occurs.

Figure 5 provides the concentration of $GnRH$ over time, it can be seen that, although there is a slight delay, around days 1 through 10, $GnRH$ is still being stimulated. Before day 1 and after day 10, $GnRH$ reaches an equilibrium showing inhibition of $GnRH$. We have to keep into consideration that $GnRH$ is also effected by C_1 and its natural decay, μ_1, and variation of these affect also the simulation of $GnRH$.

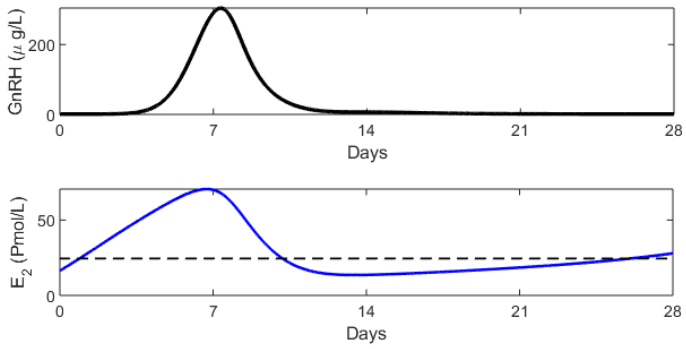

Figure 5: Concentrations of $GnRH$ by the impact of E_2.The minimum concentration of E_2 in order to stimulate $GnRH$ in the $h^{+,-}$ is shown by the dotted line provided by Table 6.

3.2.2 Impact of the threshold condition of stimulation of $GnRH$ on the system.

Let $q_1 \geq r_1$, that is that the threshold parameters of the stimulation and inhibition of $GnRH$ dependent on E_2. Then there exists an interval (q_1^{min}, q_2^{max}) such that $GnRH$ produces periodic behavior or reaches an equilibrium after a certain time, t^* as shown in equation 6.

$$\dot{GnRH}(q) = \begin{cases} periodic & \text{for } q_1^{min} \leq q \leq q_2^{max} \\ \lim_{t\to\infty} \to GnRH^*, & \text{otherwise} \end{cases} \tag{6}$$

Figure 6 shows the description of $\dot{GnRH}(q)$ on a line.

Figure 6: GnRH reaches will lose periodic behavior when $q < q_1^{min}$ or when $q > q_2^{max}$.

When $q_1 \leq q_1^{min}$ or when $q_1 \geq q_1^{max}$, $GnRH$ reaches a steady state which halts the

system as time goes to infinity as also seen in Figure 6. When $q_1 \geq q_1^{max}$ periodicity of the system will come to a halt.

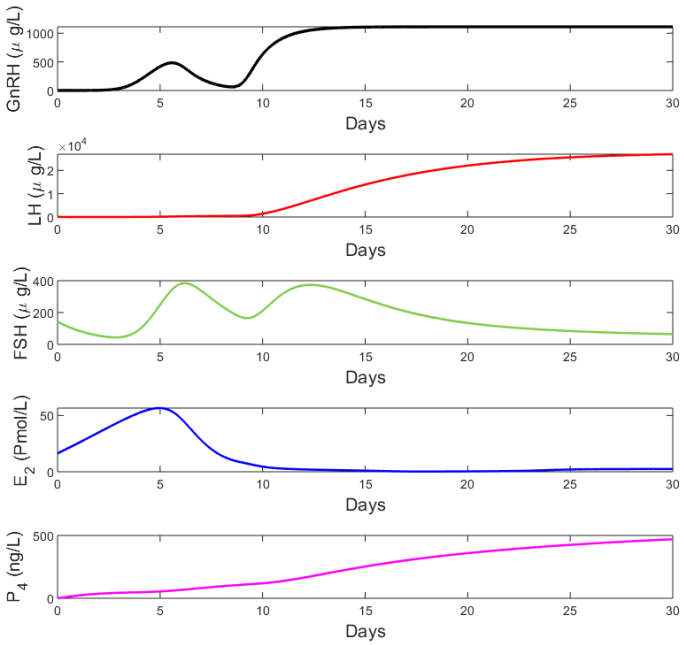

Figure 7: For $q_1 = 55$ the system will eventually reach a steady state as time goes to infinity. The dotted line in E_2 represents the minimum concentration on E_2 to stimulate $GnRH$.

Figure 7 shows the solution of 4 and the rest of the parameters are taken as Table 5 when $q_1 = 55$. It can be seen that the system eventually reaches a steady state; therefore, disrupting the system. It can also be noticed that the peak of E_2 occurs sooner and at lower levels than that seen in Figure 5 and that the peak in $GnRH$ also occurs soon and at a much smaller level. E_2 will have impact on the stimulation of $GnRH$ because it will not stimulate at the higher levels. Lower levels of $GnRH$ will lead to less stimulation of LH and FSH. Since the system shows to lose periodicity, it can be assumed that q_1 is less than q_1^{min}.

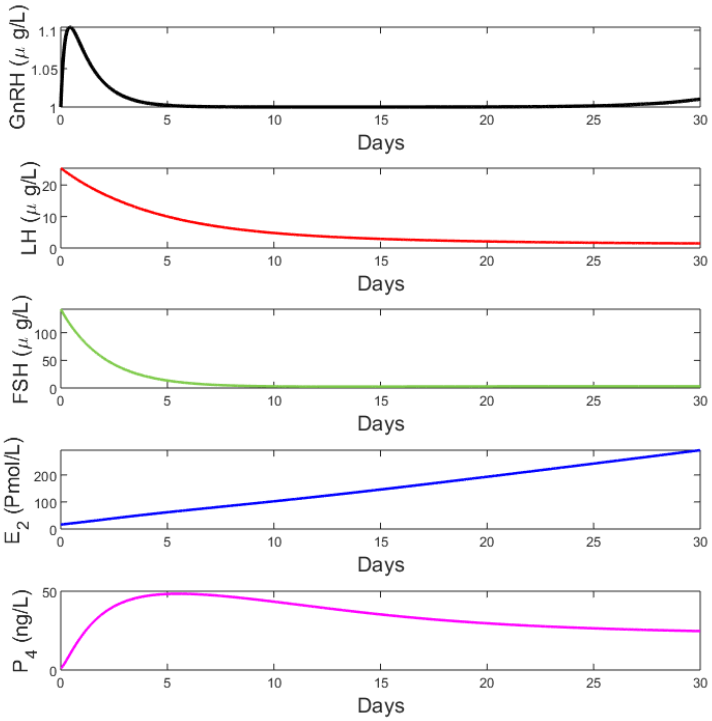

Figure 8: For $q_1 = 900$ the system reaches a steady state. The dotted line in E_2 represents the minimum concentration on E_2 to stimulate $GnRH$.

Similarly, when $q_1 = 900$, $GnRH$, LH, FSH, E_2, and P_4 lose periodicity and therefore the system goes to a halt. The time interval where E_2 stimulates $GnRH$ is larger; however, $GnRH$ decreases in the time before E_2 can stimulate. This means that E_2 will have minimal to no concentration of $GnRH$ and in turn $GnRH$ can be seen to provide not much stimulation to FSH and LH, and as a consequence leading to a decrease in $GnRH$, LH, and FSH.

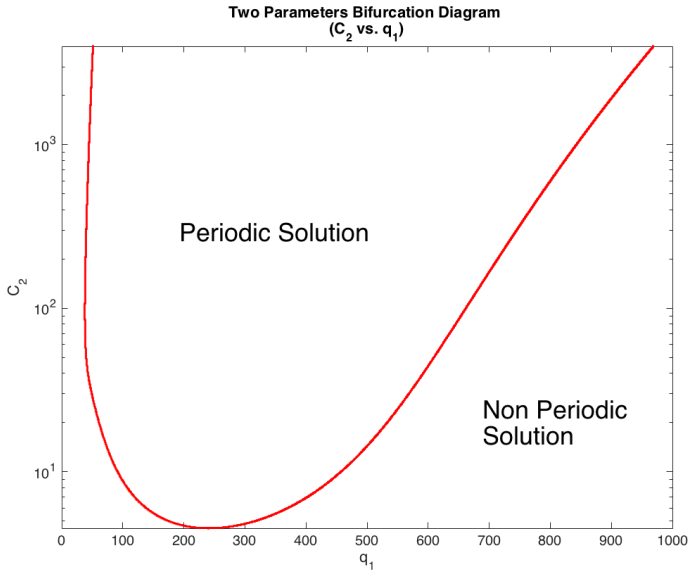

Figure 9: Hopf Bifurcation is shown for ranges of the conversion factor of $GnRH$ by ranges of the threshold value of stimulation of $GnRH$ dependent on E_2.

In order to understand within what intervals can q_1 be for there to be periodicity within the system it must be known at what point the system loses its stability. Through numerical analysis preformed using XPP-Auto we were able to find the Hopf Bifurcation, shown in Figure 9, for ranges of the conversion factor of $GnRH$, C_2, by ranges of q_1. Within the region over the line exists all values of C_1 and q_1 where periodic solutions of the system exist. Below the bifurcation curve exists all values of q_1 and C_2 where the system leads to a steady state. We only look at values within the region because it is necessary to have periodic solutions in order have periodic effects in the menstrual cycle. We can conclude from 9 that the value of C_2 gets smaller the range of q_1, where the system is periodic, gets smaller as well.

3.3 Numerical Simulation for GnRH Pulse Function

In this section, we use Equation 5 together with Equation 4b to 4f in order to built a second system of ordinary differential equations that shows periodicity behavior. This new system gives a better approximation to the behavior of the curves of concentration for all the hormones compared to the original system of differential equations. We analyze the effects of varying the width of the curve of GnRH on the curves of FSH and LH. The width of GnRH gives us a way to measure the release of GnRH by saying that as the width is larger,the levels of GnRH increases.

For this purpose, we varied the width of the $GnRH$ curve by changing g_3 (for definitions of g_i parameters see Table 3). On the other hand, we fixed the basal concentration of $GnRH$, its amplitude, and the peak time to $g_1 = 1\frac{\mu g}{L}$, $g_2 = 999\frac{\mu g}{L}$, and $g_4 = 1.78$, respectively. We use the initial conditions given as in Table 4 . Then, for LH and FSH hormones, we analyze how the width, the value of the peak, and the time at which the peak is achieved are affected as g_3 varies.

Let us denote LH_3 as the width of LH, FSH_3 as the width of FSH. We plot g_3 versus LH_3; g_3 versus the maximum concentration of FSH and LH, denoted as Max LH and Max FSH, respectively; and g_3 versus the peak time for LH and FSH(t_{max}).

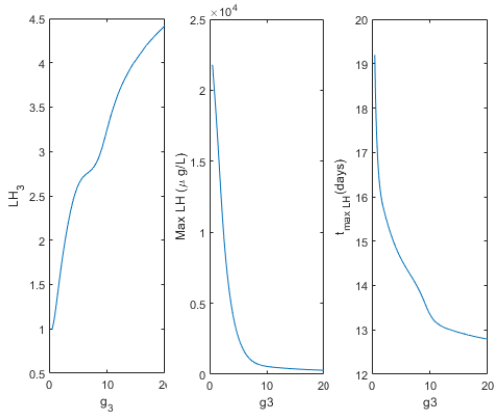

(a) (b) (c)

Figure 10: (a) g_3 vs. LH_3, shows that the increment of the width of GnRH increases the width of LH; in addition, the rate of change of LH_3 is positive respect to g_3. (b)g_3 vs. Max LH, shows that as the width of GnRH decreases (i.e. g_3 increases), the max of LH also decreases. (c) g_3 vs. t_{MaxLH}, shows that LH achieves its peak earlier as the width of $GnRH$ decreases.

In figure 10a shows that as the width of GnRH decreases, the width of LH_3 decreases as well. This effect can be seen in Figure 12 and Figure 13. On the other hand, 10b describes graphically that the decrease of width in GnRH decreases the peak of LH levels. For example, 12 and Figure 13 shows a peak of LH to be $554.9\frac{\mu g}{L}$ for $g_3 = 10$ and $2649\frac{\mu g}{L}$ for $g_3 = 5$. Moreover, Figure 10c shows that when the width of GnRH decreases, the period of time at which LH rises its peak is smaller. Additionally, since 10a is a concave graph, the rate change of LH_3 respect to g_3 is decreasing, which suggests that for larger values of g_3, LH_3 is less affected by varying g_3. Figure 10b and 10c suggest that for larger values of g_3m Max LH and t_{MaxLH} varies very little. (Two examples are shown in Figure 12 and Figure 13.)

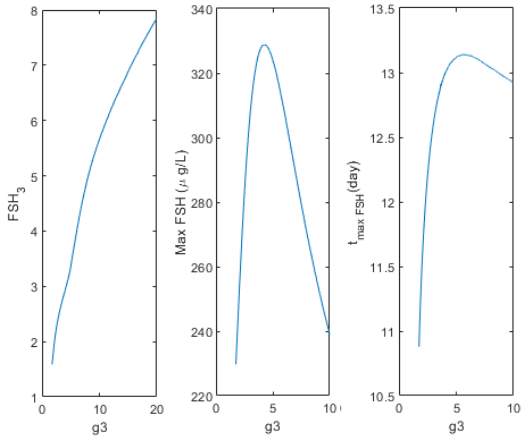

(a) (b) (c)

Figure 11: In (a), g_3 vs. FSH_3, we can see that the decrease of the width of GnRH decreases the width of FSH. (b) g_3 vs. Max FSH, shows that there is a maximum at $g_3 = 10$ for Max FSH. (c) g_3 vs. t_{maxFSH}, shows that FSH achieves its peak earlier as the width of GnRH increases, but there is also small width of GnRH that decreases the time at which the maximum peak is achieved.

Figure 11 shows three different graphs. Figure 11a , g_3 vs. FSH_3, shows that the width of FSH increases as g_3 increases.We can see two examples in Figure 12 and Figure 13 were it is shown a peak of FSH at $813.2\frac{\mu g}{L}$ for $g_3 = 10$ and $677.3\frac{\mu g}{L}$ for $g_3 = 5$. However, in contrast to the case of LH, the rate of change of width of FSH respect to g_3 is positive. In addition, Figure 11b represents the impact of GnRH width on the maximum level of FHS. This image shows a concave graph of Max FSH vs. g_3, achieving its maximum at $g_3 = 10$. For this reason, there is a region around this values where the peaks of FSH decreases by varying g_3. Moreover, looking at Figure 11c we can see that there is two local maxima and one local minimum at $g_3 = 4.25$, $g_3 = 10.75$, and $g_3 = 5.55$, respectively. We can see that between the two maxima there is a huge variation in the values of t_{maxFSH}. Also, for values smaller than $g_3 = 10$, changes in g_3 will affect more the value of t_{maxFSH} than for values greater than 10.

Additionally, we also performed a numerical simulation that shows the levels of each hormone during a period of 28 days using Equation 5 together with Equations 4b to 4f. The results are presented in Figure 12 and Figure 13. These graphs show the sinusoidal behavior of $GnRH$, LH, and FSH. We can see that this model give us a much better peak time of $GnRH$, LH, and FSH compared with those of Figure 4.

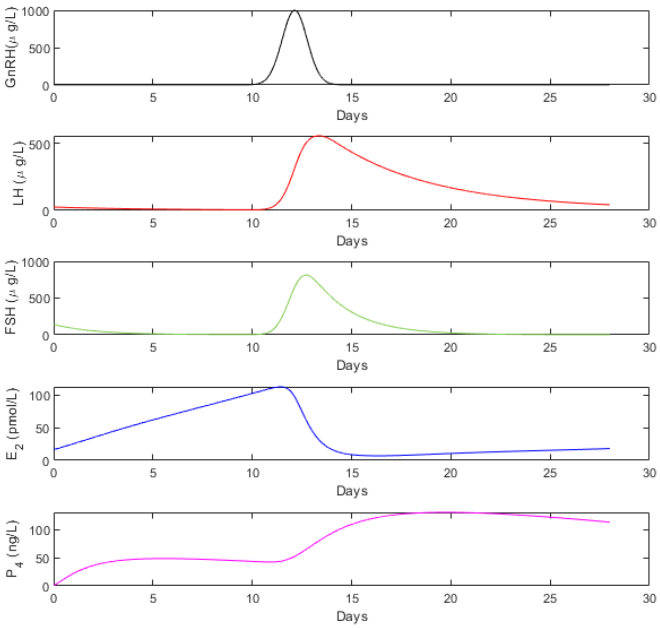

Figure 12: Numerical simulation for the effect of the width of $GnRH(t)$ ($g_3 = 10$) in the other hormones producing pulses on all.

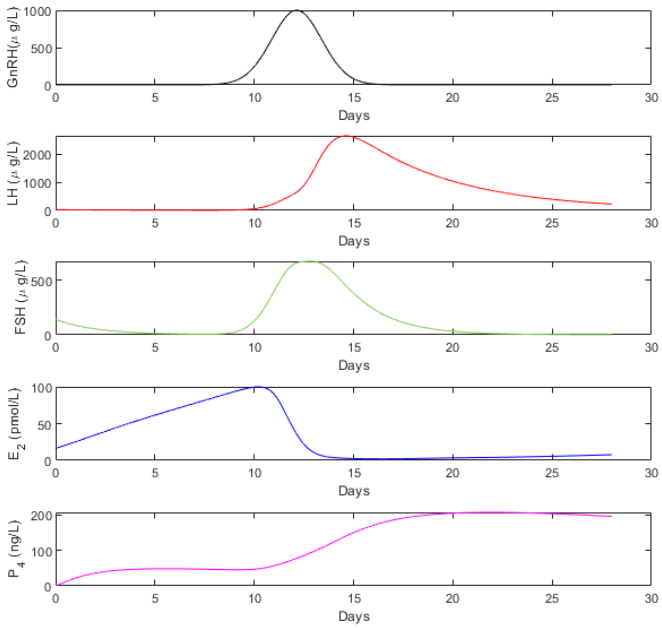

Figure 13: Numerical simulation for the effect of the width of $GnRH(t)$ ($g_3 = 5$) in the other hormones producing pulses on all.

4 Sensitivity Analysis

Sensitivity analysis (SA) determines how changes in an input, e.g. a parameter value or an initial condition of variables of a model affects changes in its output [3]. SA considers the ratio between the output perturbation and input perturbation given by:

$$S_p := \frac{||\alpha||}{||H||}\frac{\partial H}{\partial \alpha} \tag{7}$$

where $H \neq 0$, α is a parameter, and H is an output of interest.

For this research, local sensitivity analysis of parameters was performed using the parameter values from literature, Table 5, and from parameter estimation, Table 6. In particular, sensitivity analysis to the solutions of the model per day was performed for values that affect the production of $GnRH$, i.e. r_1 and q_1.

The objective of sensitivity analysis is to understand the qualitative behavior of $GnRH$ effects on LH, FSH, E_2, and P_4. The SA to D will not be considered for this analysis given that it is a precursor to P_4. The parameters considered for the analysis are r_1 and q_1 from Equation 4a. The parameter r_1 represents the threshold concentration value of E_2 that controls the inhibition mechanism for $GnRH$, and q_1 represents the threshold concentration value of E_2 that controls the stimulation mechanism for $GnRH$. Qualitatively, these two parameters are those that affect the rate of change of $GnRH$ the most and their sensitivity comes from the fact that they are the two parameters within the biphase Hill function in Equation 4a.

Eighteen ordinary differential equations were taken into account: six equations come

from the Forward Problem (FP) (Equations 4a to 4e); and twelve equations from the Forward Sensitivity Equations (FSE). To get the FSE we use partial derivatives of the steady state with respect to r_1 and q_1. For the calculations of the sensitivity indexes of Equations 4a to 4e see Appendix B.

To find the initial conditions for the twelve Forward Sensitivity Equations we take the sensitivity index equal to one at $t = 0$, i.e.,

$$\left(\frac{\alpha}{H}\frac{\partial H}{\partial \alpha}\right)\Big|_{t=0} = 1. \tag{8}$$

The system of ODE's with twelve equations was solved using the *NDSolve* function on the software *Mathematica*. The SA results for the parameters obtained in literature are shown in Figure 14.

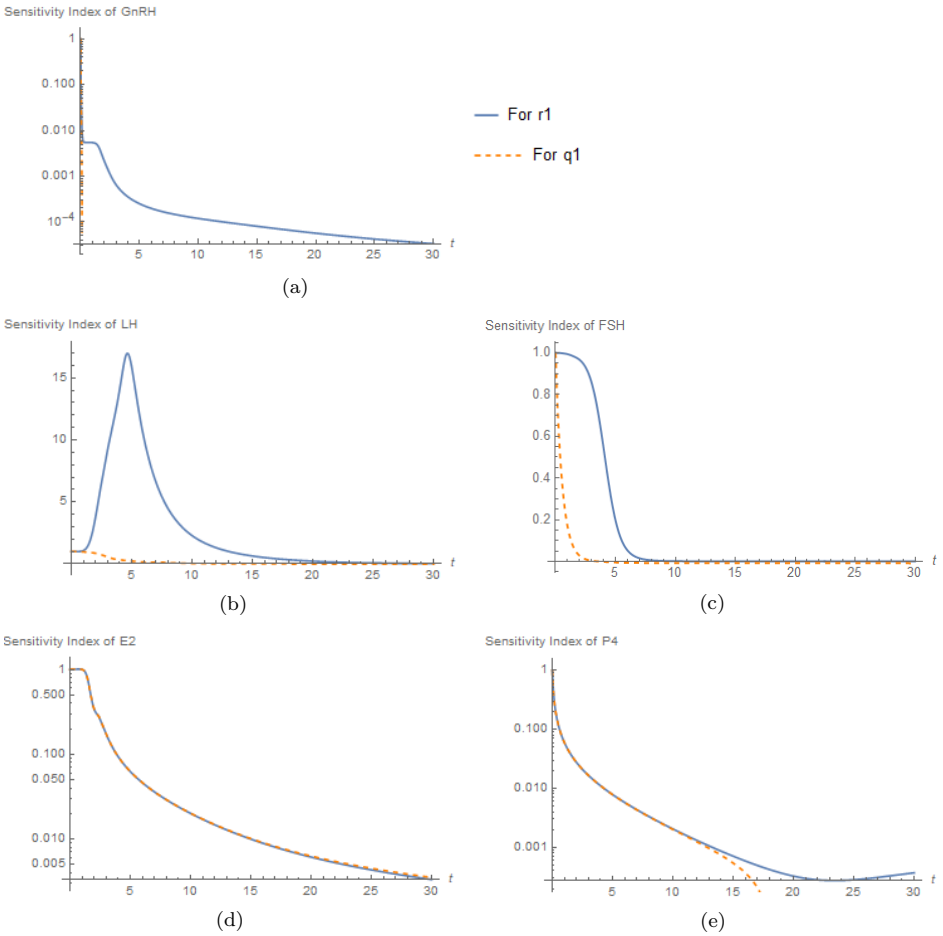

Figure 14: Sensitivity indexes of $GnRH$, LH, FSH, E_2, and P_4 respectively with respect to r_1 and q_1 as time changes using parameters given in Table 5.

The simulation of the sensitivity analysis of the system using the parameters given in the literature show no significant changes in solutions according to how the values of r_1 and q_1 change. For example, for the parameter values given in Table 5, the impact of changing values r_1 and q_1 are more significant for FSH and E_2. However, in both

cases, the sensitivity indexes are positive, meaning that increasing r_1 and q_1 values by 1% will increase E_2 and FSH. However, as time progresses, after 8 days, the impact that r_1 and q_1 have on both FSH and E_2 diminishes until eventually there is no effect.

It is important to note that the sensitivity analysis with respect to the literature parameters in Table 5 do not accurately reflect the expected periodic behavior of the hormones. Equations 4a to 4e are made up of feedback mechanisms meaning that the five hormones $GnRH$, LH, FSH, E_2, and P_4 all have negative and positive impacts on the concentration of one another. Therefore, it is evident that the parameters used must be adjusted to achieve the expected qualitative and quantitative results, as was done in Section 3.1

Through parameter estimation, the values in Table 6 were then used to accurately reflect the expected behavior of the model. The results of SA are shown in Figure 15.

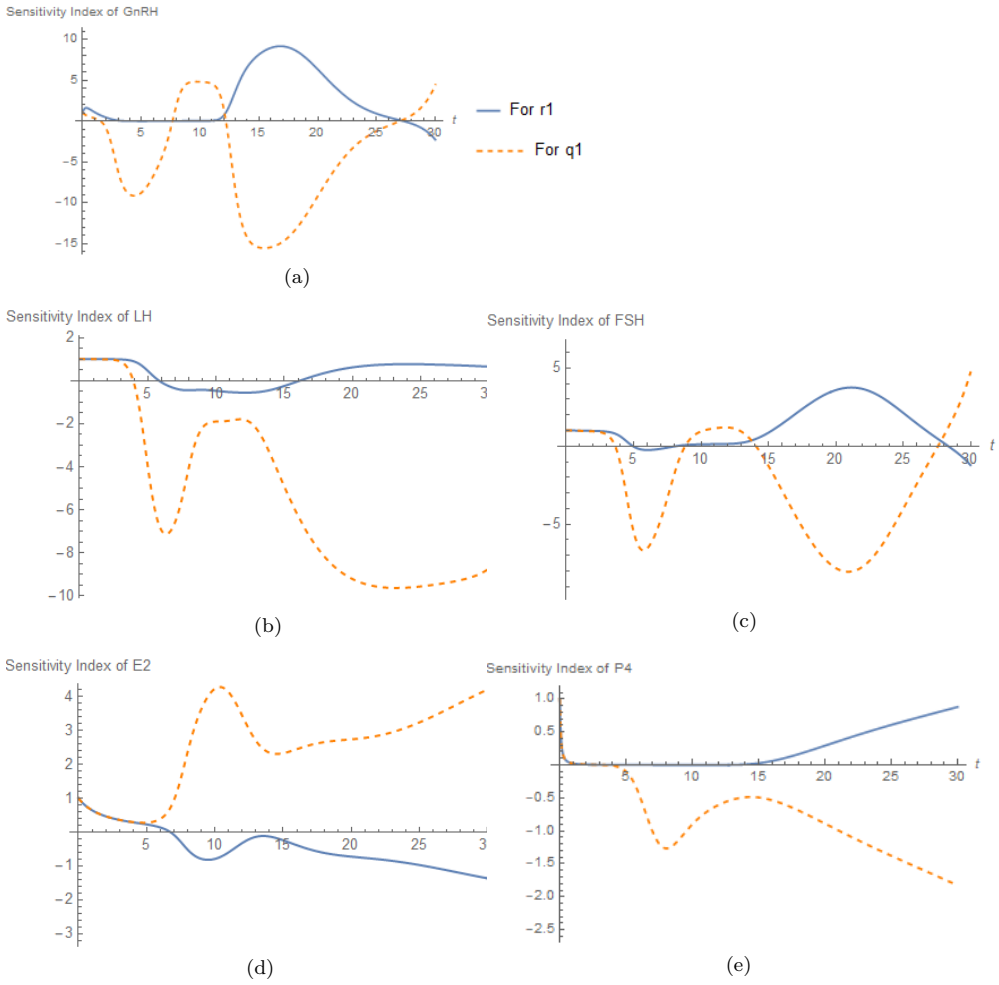

Figure 15: Sensitivity Index of $GnRH$, LH, FSH, E_2, and P_4, in (a) to (e), respectively. Sensitivity Analyses with respect to r_1 and q_1 as time changes using parameters given in Table 6.

Figures 15a to 15e show that all hormones are highly sensitive to changes in r_1 and q_1 with a set of parameter values that replicate the qualitative behavior of the hormones

in the menstrual cycle. Figure 15a illustrates how the sensitivity indexes of $GnRH$ change with time for r_1 and q_1. Recall that r_1 and q_1 are the threshold concentration values with respect to E_2 that inhibit and stimulate $GnRH$, respectively. It was found that $GnRH$ is sensitive to changes of r_1 and q_1 when $0 < t < 1$ day, but sensitive to r_1 by a greater magnitude when $11 < t < 27$ days. This means that when r_1 and q_1 are increased by 1%, the concentration of $GnRH$ increases by 1% for the first time period, but increases between 1% to 10% for $11 < t < 27$ days when r_1 increases. On the other hand, 15a suggests that $GnRH$ is sensitive to q_1 on a greater magnitude than r_1, and that $GnRH$ is sensitive to q_1 at all times.

When $1 < t < 7$ days, if q_1 is raised by 1%, then $GnRH$ will decrease between 1% to 10%. Given that $GnRH$ is vital during the follicular stage for the induction of the menstrual cycle, $GnRH$ would be highly sensitive to changes in threshold concentration values during the beginning of the menstrual cycle since certain levels of E_2 are needed to stimulate $GnRH$. From Figure 4, we observe that E_2 levels are only beginning to rise at about this time as q_1 increases, so if the threshold concentration value that stimulates $GnRH$ is increased, it will be difficult for E_2 to reach that increased value, thus preventing $GnRH$ from increasing. However, after the follicular phase, when $7 < t < 12$ days, $GnRH$ has already signaled the release of LH and FSH which also leads to the increase in concentration of E_2. Since E_2 levels are now high at this point, and if q_1 is increased by 1%, then $GnRH$ will be stimulated, leading to the increase in concentration by about 5%. The trend changes once again after 12 days when E_2 has decreased (see Figure 4), implying once again that if q_1 is increased, E_2 will be unable to stimulate $GnRH$, thus allowing $GnRH$ to decrease from 1% to 15%. Additionally, E_2 increases at the end of the cycle during the luteal phase, meaning that if q_1 is increased by 1%, it is possible for $GnRH$ to increase by about 5%. This lends to a greater understanding as to how levels of E_2 greatly affect $GnRH$ and at what time periods.

Considering the sensitivity index of LH with respect to changes in r_1 and q_1, (see Figure 15b), the change in q_1 has a greater effect on LH compared to the effect caused by the change in r_1. For $0 < t < 6$ days, if r_1 is increased by 1%, then the concentration of LH will increase by about 1%. However, the relationship transitions for $6 < t < 16$ days such that increasing r_1 will decrease LH by about 0.5%. Furthermore, after 16 days, increasing r_1 will increase LH by 1%. This analysis shows that changes in the threshold concentration value for E_2 that inhibits $GnRH$ has a very small effect on the concentration of LH, meaning that if $GnRH$ is inhibited, LH will still be released. On the other hand, since the sensitivity index with respect to q_1 is negative after 4 days, if q_1 increases by 1%, LH will decrease by up to 9%. The magnitude is less for $8 < t < 13$ days when the concentration of E_2 is decreasing. However, at this point, LH has already increased towards its maximum concentration value (see Figure 4), meaning that increasing the threshold concentration value that stimulates $GnRH$ will decrease the concentration of LH on a smaller magnitude given that LH is already increasing. Additionally, if q_1 is increased, recall that $GnRH$ will be prevented from increasing for most of the 30 day period. Similarly, LH will also decrease during this time period. This shows that the release of $GnRH$ leads to the release of LH, suggesting that when it is difficult for E_2 to meet its threshold concentration value required for $GnRH$ stimulation, LH will also be released at much lower concentrations.

In the case of FSH, the sensitivity index with respect to r_1 and q_1 is very similar to that of $GnRH$ (see Figure 15c). However, the time periods are shifted which suggests that there is a time period accounted for when $GnRH$ is signaling to the release of FSH. This is also observed in Figure 4 in which the peak of FSH occurs after the $GnRH$ peak. In Figure 15c, for $0 < t < 4$ days, if r_1 and q_1 are increased by 1%, FSH will increase by 1%. Additionally, for $4 < t < 9$ days, if q_1 is increased by 1%, FSH will decrease up to 7% which is 3% less than what $GnRH$ would decrease by at this

time. This trend continues, such that FSH is sensitive to changes in q_1 on a greater magnitude compared to r_1. Although the time periods for high sensitivity are shifted in Figure 15c compared to 15a, this indicates that FSH is dependent on E_2 in the same manner as $GnRH$ because the release of FSH is induced by $GnRH$. Additionally, FSH is sensitive to changes in r_1 and q_1 to a smaller magnitude because $GnRH$ acts as an intermediary stage, meaning that the effect of E_2 on FSH is lessened due to the direct relationship between $GnRH$ and FSH.

The sensitivity index of E_2 with respect to r_1 and q_1 are nearly opposite to that of $GnRH$, LH, FSH, and P_4. Observe that whenever q_1 is increased, E_2 will also increase. This is because if the threshold concentration value needed to stimulate $GnRH$ is raised, levels of E_2 will increase in order to fulfill its role as a hormone. Observe that for $0 < t < 5$ days, if q_1 is raised by 1%, then E_2 increases up to 1%. This percentage is small because E_2 has already began to increase, meaning that it is possible for E_2 to account for the increase in q_1. Notice that the sensitivity magnitude with respect to q_1 is much greater for $7 < t < 14$ days. At this time period, the menstrual cycle is preparing for ovulation, implying that hormones are required to be at certain levels during stage transitions. Therefore, changing threshold concentration values will extremely affect E_2 which is needed to regulate $GnRH$ which regulates the other hormones based on the feedback mechanisms observed in System 4. Moreover, E_2 is also highly sensitive to changes in both r_1 and q_1 during the luteal phase and towards the end of the menstrual cycle. This is because at this point, the concentration of E_2 needs to increase in order to prepare for the follicular phase when $GnRH$ is required to induce the menstrual cycle once again.

Figure 15e illustrates the sensitivity index of P_4 with respect to r_1 and q_1. For $0 < t < 1$ day, if r_1 and q_1 are increased by 1% then P_4 also increases by about 1%. This suggests that at this time period, the inhibition and stimulation of $GnRH$ caused by E_2 greatly affect the change in concentration of P_4. After 1 day, r_1 has little effect on P_4 until about day 15 when the sensitivity index begins to rise, meaning that increasing r_1 by 1% increases P_4 by up to 1%. For $15 < t < 30$ days, P_4 raises between 0.1% to 0.9%. Ultimately, P_4 is highly sensitive to q_1, such that at any point after day 5, if q_1 is raised by 1%, P_4 decreases by up to 2%. When the threshold concentration value of E_2 that stimulates $GnRH$ is increased, P_4 is prevented from increasing, just as $GnRH$ is prevented for most of the 30 day period if q_1 increases. If the concentration of $GnRH$ decreases, then so does P_4. This confirms our understanding of the menstrual cycle such that the release of $GnRH$ leads to the release of P_4. Thus, the increase of P_4 is highly dependent on both E_2 and $GnRH$ suggesting that if a woman has usually low or high progesterone levels, then the cause may be due to irregular regulation of E_2.

Altogether, the sensitivity analysis reflects the expected variations in concentration over time of $GnRH$, LH, FSH, E_2, and P_4 when the threshold concentration values of E_2 that control the stimulation and inhibition of $GnRH$ are varied. We are able to conclude that the hormones are sensitive to r_1 and q_1, but they are affected by q_1, the threshold concentration value of E_2 that stimulates $GnRH$, to a greater extent. Through this analysis, we observe how r_1 and q_1 affect $GnRH$, LH, FSH, E_2 and P_4 and at what time periods these hormones are most sensitive. Ultimately, by observing all sensitivity indexes with respect to the parameter values from Table 6, it is evident that the hormones are extremely sensitive to the change in r_1 and q_1 during phase shifts. These changes are observable at the end of the follicular phase. It is plausible that the concentration of hormones would be highly sensitive at this point because the menstrual cycle is preparing for ovulation which occurs during the middle of the cycle. Similarly, sensitivity is high for all hormones at the end of the luteal phase which occurs right before the female body begins another menstrual cycle. It is unsurprising that these dynamics would occur at phase shifts given that hormones are required to be at certain

levels in order to properly induce each the follicular phase, ovulation, and the luteal phase.

5 Conclusion

The complexities of the menstrual cycle were captured by the decomposition of two independent studies into six non-linear differential equations to model the dynamics of hormonal regulation over a 30-day period. As parameter estimation was challenging, simulations and analyses were performed in order for the model to reflect the qualitative behavior and essential characteristics of hormone levels during the menstrual cycle.

Simulations of the model were performed to understand how changes in parameters in the differential equation for $GnRH$ impact the disturbances in the behavior of LH, FSH, E_2, and P_4. By analyzing these disturbances and utilizing the necessary parameter values of $GnRH$ for our model, we showed how sensitive the system behaved when parameter values were not in the appropriate range. This illustrated how the behavior of the hormones changed drastically when $GnRH$ parameters were altered.

In addition, by using our second model which consider Equation 5, we conclude that since the larger width of $GnRH$ represents high levels of $GnRH$ for larger period of time, Figure 10 suggests that a larger time interval expositions to $GnRH$ produces a larger time interval production of LH, and at the same time increases the maximum levels of LH. Specifically, the 10c suggests that decreasing the width of $GnRH$ decreases drastically the time of maximum release of LH, and consequently will affect the time at which the production of P_4 and E_2 happens. In addition, Figure 11a shows that if the concentration of $GnRH$ per day decreases, the concentration of FSH per day also decreases. Moreover, in Figure 11b as the $GnRH$ concentration decreases, the maximum level of FSH concentration increases until certain value corresponding to $g_3 = 10$. Moreover, Figure 11c shows that higher concentrations of $GnRH$ for larger interval of time produces huge variations in the time of maximum release of FSH. In general, comparing the shapes of Figure 11 and Figure 10 we suggest that FSH is more affected than LH by changes of $GnRH$ concentration. In general, comparing the shapes of Figure 11 and Figure 10 we suggest that FSH is more affected than LH by changes of $GnRH$ concentration.

In addition, we performed a sensitivity analysis that revealed the effect of the two parameters, q_1 and r_1 that directly affect the change in concentration of $GnRH$, provided that they are the threshold values that determine the output of $GnRH$. The sensitivity analysis showed that the threshold conditions of E_2 that inhibit and stimulate $GnRH$ played a significant role on the production of the hormones. Ultimately this led to a strong understanding of not only how our model behaves, but also how sensitive each hormone is during specific time intervals. Sensitivity levels are significantly higher before ovulation and the follicular stage which shows how both r_1 and q_1 are required to be within the correct range in order for hormones to be at the vital concentrations for the menstrual cycle to occur as expected. Additionally, sensitivity varies during certain time periods which suggests that any treatment for menstrual irregularity would be highly dependent on timing of dosages.

In creating a model that qualitatively captured the hormonal behavior in the menstrual cycle that was still simple enough to better interpret relationships between $GnRH$, LH, FSH, E_2, and P_4, we were able to capture results that could be helpful in hormonal therapies. By identifying time intervals during which certain hormonal changes are more drastic, it is possible to better regulate when treatment delivery will be more efficient. Future studies can use this model as a basis for further research on external influences of $GnRH$.

6 Acknowledgments

We would like to thank Dr. Carlos Castillo-Chavez, Founding and Co-Director of the Mathematical and Theoretical Biology Institute (MTBI), for giving us the opportunity to participate in this research program. We would also like to thank Co-Director Dr. Anuj Mubayi as well as Coordinator Ms. Rebecca Perlin and Management Intern Ms. Sabrina Avila for their efforts in planning and executing the day to day activities of MTBI. We also want to give special thanks to Leon Arriola for his expertise. This research was conducted as part of 2018 MTBI at the Simon A. Levin Mathematical, Computational and Modeling Sciences Center (MCMSC) at Arizona State University (ASU). This project has been partially supported by grants from the National Science Foundation (NSF Grant MPS-DMS-1263374 and NSF Grant DMS-1757968), the National Security Agency (NSA Grant H98230-J8-1-0005), the Office of the President of ASU, and the Office of the Provost of ASU.

A Appendix

A.1 Tables

Table 5: Parameter values of the system of ordinary differential equations given by literature

Parameter	Value	Units	Reference
C_1	433.3447	$\frac{\mu g}{d}$	[9]
C_2	102.4000	$\frac{\mu g}{d}$	[9]
C_3	16.3680	$\frac{1}{d}$	[9]
C_4	16.6120	$\frac{1}{d}$	[9]
C_5	186.3917	$\frac{ng/L}{d}$	[5]
C_6	4.4833	$\frac{1}{d}$	[5]
C_7	202.2639	$\frac{ng/L}{d}$	[5]
C_8	1.0303	$\frac{1}{d}$	[5]
C_9	0.8848	$\frac{1}{d}$	[5]
C_{10}	0.0715	$\frac{L}{\mu g * d}$	[5]
C_{11}	0.9795	$\frac{nmol/L}{d}$	[5]
n_1	1.0000	unitless	[9]
n_2	1.0000	unitless	[9]
n_3	1.0000	unitless	[9]
n_4	1.0000	unitless	[9]
n_5	1.0000	unitless	[9]
n_6	0.9994	unitless	[9]
n_7	1.0010	unitless	[9]
n_8	0.9996	unitless	[9]
n_9	1.0000	unitless	[9]
n_{10}	4.0000	unitless	[5]
n_{11}	4.0000	unitless	[5]
n_{12}	4.0000	unitless	[5]
n_{13}	4.0000	unitless	[5]
n_{14}	4.0000	unitless	[5]
n_{15}	4.0000	unitless	[5]
q_1	207.8000	$\frac{ng}{L}$	[9]
q_2	348.8000	$\frac{ng}{L}$	[9]
q_3	1.3010	$\frac{nmol}{L}$	[9]
q_4	638.8000	$\frac{U}{L}$	[9]
q_5	0.3118	$\frac{ng}{L}$	[9]
q_6	115.0282	$\frac{\mu g}{L}$	[5]
q_7	200.5842	$\frac{ng}{L}$	[5]
q_8	0.3265	$\frac{nmol}{L}$	[5]
q_9	0.0897	$\frac{nmol}{L}$	[5]
r_1	7.8290	$\frac{ng}{L}$	[9]
r_2	0.04647	$\frac{ng}{L}$	[9]
r_3	4.1590	$\frac{nmol}{L}$	[9]
r_4	42.0900	$\frac{ng}{L}$	[9]
r_5	3.4154	$\frac{\mu g}{L}$	[5]
r_6	3.8448	$\frac{nmol}{L}$	[5]
α	1.4030	$\frac{U}{ng}$	
β	21.5474	$\frac{U}{nmol}$	
μ_1	26.7584	$\frac{1}{d}$	[9]
μ_2	15.7300	$\frac{1}{d}$	[9]
μ_3	1.7790	$\frac{1}{d}$	[9]
μ_4	0.2590	$\frac{1}{d}$	[5]

Table 6: Parameter values of the system of ordinary differential equations solved using parameter estimation.

Parameter	Value	Units	References
C_1	0.9	$\frac{\mu g}{d}$	
C_2	1000	$\frac{\mu g}{d}$	
C_3	5.3	$\frac{1}{d}$	
C_4	5.9	$\frac{1}{d}$	
C_5	2.39	$\frac{ng/L}{d}$	
C_6	2	$\frac{1}{d}$	
C_7	8.26	$\frac{ng/L}{d}$	
C_8	1	$\frac{1}{d}$	
C_9	1.47	$\frac{1}{d}$	
C_{10}	5.5	$\frac{L}{\mu g * d}$	
C_{11}	2.9695	$\frac{nmol/L}{d}$	
n_1	10	unitless	
n_2	10	unitless	
n_3	2	unitless	
n_4	2	unitless	
n_5	2	unitless	
n_6	2	unitless	
n_7	2	unitless	
n_8	2	unitless	
n_9	2	unitless	
n_{10}	2	unitless	
n_{11}	2	unitless	
n_{12}	2	unitless	
n_{13}	4	unitless	[9]
n_{14}	4	unitless	[9]
n_{15}	4	unitless	[9]
q_1	75	$\frac{ng}{L}$	
q_2	125	$\frac{ng}{L}$	
q_3	100	$\frac{nmol}{L}$	
q_4	7	$\frac{U}{L}$	
q_5	50	$\frac{ng}{L}$	
q_6	500	$\frac{\mu g}{L}$	
q_7	1.58	$\frac{ng}{L}$	
q_8	110.6	$\frac{nmol}{L}$	
q_9	0.089	$\frac{nmol}{L}$	[9]
r_1	8	$\frac{ng}{L}$	
r_2	20	$\frac{ng}{L}$	
r_3	700	$\frac{nmol}{L}$	
r_4	20	$\frac{ng}{L}$	
r_5	90.415	$\frac{\mu g}{L}$	
r_6	5.844	$\frac{nmol}{L}$	
α	1.4030	$\frac{U}{ng}$	
β	21.5474	$\frac{U}{nmol}$	
μ_1	0.9	$\frac{1}{d}$	
μ_2	0.2	$\frac{1}{d}$	
μ_3	0.5	$\frac{1}{d}$	
μ_4	0.89	$\frac{1}{d}$	

Table 7: Initial values of the state variables of the system of ordinary differential equations taking from experimental data.

State Variables	Definition	Value	Unit	Reference
GnRH	Gonadotropin Release Hormone	1.201	$\frac{\mu g}{L}$	[9]
LH	Luteinizing Hormone	4.465	$\frac{\mu g}{L}$	[9]
FSH	Follicular Stimulating Hormone	52.34	$\frac{\mu g}{L}$	[9]
E2	Estradiol	35.4756	$\frac{ng}{L}$	[5]
P4	Progesterone	1.5793	$\frac{nmol}{L}$	[5]
D	Precursor	1.000	$\frac{nmol}{L}$	

B Forward Sensitivity Equations

Consider,

$$\frac{dGnRH}{dt} = f_1(E_2, GnRH), \tag{9}$$

$$\frac{dLH}{dt} = f_2(E_2, P_4, GnRH, LH), \tag{10}$$

$$\frac{dFSH}{dt} = f_3(E_2, P_4, GnRH, FSH), \tag{11}$$

$$\frac{dE_2}{dt} = f_4(FSH, LH, E_2, P_4), \tag{12}$$

$$\frac{dP_4}{dt} = f_5(D, P_4), \tag{13}$$

$$\tag{14}$$

Then, our Forward Sensitivity Equations is given by,

$$\frac{d}{dt}\frac{\partial GnRH}{\partial r_1} = \frac{\partial f_1}{\partial GnRH}\frac{\partial GnRH}{\partial r_1} + \frac{\partial f_1}{\partial E_2}\frac{\partial E_2}{\partial r_1} + \frac{\partial f_1}{\partial r_1} \tag{15}$$

$$\frac{d}{dt}\frac{\partial GnRH}{\partial q_1} = \frac{\partial f_1}{\partial GnRH}\frac{\partial GnRH}{\partial q_1} + \frac{\partial f_1}{\partial E_2}\frac{\partial E_2}{\partial q_1} + \frac{\partial f_1}{\partial q_1} \tag{16}$$

$$\frac{d}{dt}\frac{\partial LH}{\partial r_1} = \frac{\partial f_2}{\partial E_2}\frac{\partial E_2}{\partial r_1} + \frac{\partial f_2}{\partial P_4}\frac{\partial P_4}{\partial r_1} + \frac{\partial f_2}{\partial GnRH}\frac{\partial GnRH}{\partial r_1} + \frac{\partial f_2}{\partial LH}\frac{\partial LH}{\partial r_1} + \frac{\partial f_2}{\partial r_1} \tag{17}$$

$$\frac{d}{dt}\frac{\partial LH}{\partial q_1} = \frac{\partial f_2}{\partial E_2}\frac{\partial E_2}{\partial q_1} + \frac{\partial f_2}{\partial P_4}\frac{\partial P_4}{\partial r_1} + \frac{\partial f_2}{\partial GnRH}\frac{\partial GnRH}{\partial r_1} + \frac{\partial f_2}{\partial LH}\frac{\partial LH}{\partial q_1} + \frac{\partial f_2}{\partial q_1} \tag{18}$$

$$\frac{d}{dt}\frac{\partial FSH}{\partial r_1} = \frac{\partial f_3}{\partial E_2}\frac{\partial E_2}{\partial r_1} + \frac{\partial f_3}{\partial P_4}\frac{\partial P_4}{\partial r_1} + \frac{\partial f_3}{\partial GnRH}\frac{\partial GnRH}{\partial r_1} + \frac{\partial f_3}{\partial FSH}\frac{\partial FSH}{\partial r_1} + \frac{\partial f_3}{\partial r_1} \tag{19}$$

$$\frac{d}{dt}\frac{\partial FSH}{\partial q_1} = \frac{\partial f_3}{\partial E_2}\frac{\partial E_2}{\partial q_1} + \frac{\partial f_3}{\partial P_4}\frac{\partial P_4}{\partial r_1} + \frac{\partial f_3}{\partial GnRH}\frac{\partial GnRH}{\partial r_1} + \frac{\partial f_3}{\partial FSH}\frac{\partial FSH}{\partial q_1} + \frac{\partial f_3}{\partial q_1} \tag{20}$$

$$\frac{d}{dt}\frac{\partial E_2}{\partial r_1} = \frac{\partial f_4}{\partial E_2}\frac{\partial E_2}{\partial r_1} + \frac{\partial f_4}{\partial P_4}\frac{\partial P_4}{\partial r_1} + \frac{\partial f_4}{\partial LH}\frac{\partial LH}{\partial r_1} + \frac{\partial f_4}{\partial FSH}\frac{\partial FSH}{\partial r_1} + \frac{\partial f_4}{\partial r_1} \tag{21}$$

$$\frac{d}{dt}\frac{\partial E_2}{\partial q_1} = \frac{\partial f_4}{\partial E_2}\frac{\partial E_2}{\partial q_1} + \frac{\partial f_4}{\partial P_4}\frac{\partial P_4}{\partial q_1} + \frac{\partial f_4}{\partial LH}\frac{\partial LH}{\partial q_1} + \frac{\partial f_4}{\partial FSH}\frac{\partial FSH}{\partial q_1} + \frac{\partial f_4}{\partial q_1} \tag{22}$$

$$\frac{d}{dt}\frac{\partial P_4}{\partial r_1} = \frac{\partial f_5}{\partial P_4}\frac{\partial P_4}{\partial r_1} + \frac{\partial f_5}{\partial D}\frac{\partial D}{\partial r_1} + \frac{\partial f_5}{\partial r_1} \tag{23}$$

$$\frac{d}{dt}\frac{\partial P_4}{\partial q_1} = \frac{\partial f_5}{\partial P_4}\frac{\partial P_4}{\partial q_1} + \frac{\partial f_5}{\partial D}\frac{\partial D}{\partial q_1} + \frac{\partial f_5}{\partial q_1} \tag{24}$$

$$\frac{d}{dt}\frac{\partial D}{\partial r_1} = \frac{\partial f_6}{\partial LH}\frac{\partial LH}{\partial r_1} + \frac{\partial f_6}{\partial D}\frac{\partial D}{\partial r_1} + \frac{\partial f_6}{\partial r_1} \tag{25}$$

$$\frac{d}{dt}\frac{\partial D}{\partial q_1} = \frac{\partial f_6}{\partial LH}\frac{\partial LH}{\partial q_1} + \frac{\partial f_6}{\partial D}\frac{\partial D}{\partial q_1} + \frac{\partial f_6}{\partial q_1} \tag{26}$$

Forward Sensitivity Equations where $f_1, f_2, f_3, f_4, and f_5$ represents the ordinary differential equations for $GnRH$, LH, FSH, E_2, and P_4 respectively.

References

[1] *Menstrual cycle: What's normal, what's not.* https://www.mayoclinic.org/healthy-lifestyle/womens-health/in-depth/menstrual-cycle/art-20047186. Accessed: 2018-7-11.

[2] *Population, female.* https://data.worldbank.org/indicator/SP.POP.TOTL.FE.ZS?locations=US. Accessed: 2018-7-11.

[3] L. Arriola and J. M. Hyman, *Sensitivity analysis for uncertainty quantification in mathematical models*, in Mathematical and Statistical Estimation Approaches in Epidemiology, Springer, 2009, pp. 195–247.

[4] V. E. Beshay and B. R. Carr, *Hypothalamic–pituitary–ovarian axis and control of the menstrual cycle*, in Clinical Reproductive Medicine and Surgery, Springer, 2017, pp. 1–17.

[5] J. A. Brueggemann, *Numerical Modelling of the human menstrual cycle applied to ovulation prediction*, PhD thesis, University of Trier, 2013.

[6] L. M. Caronia, C. Martin, C. K. Welt, G. P. Sykiotis, R. Quinton, A. Thambundit, M. Avbelj, S. Dhruvakumar, L. Plummer, V. A. Hughes,

ET AL., *A genetic basis for functional hypothalamic amenorrhea*, New England Journal of Medicine, 364 (2011), pp. 215–225.

[7] C. CHEN AND J. P. WARD, *A mathematical model for the human menstrual cycle*, Mathematical medicine and biology: a journal of the IMA, 31 (2014), pp. 65–86.

[8] S. MELMED, *Williams textbook of endocrinology*, Elsevier Health Sciences, 2016.

[9] I. REINECKE AND P. DEUFLHARD, *A complex mathematical model of the human menstrual cycle*, Journal of Theoretical Biology, 247 (2007), pp. 303–330.

[10] I. ZOBAN, *Human menstrual cycle modeling: A review*, International Journal of Engineering Research and Technology, 7 (2018).